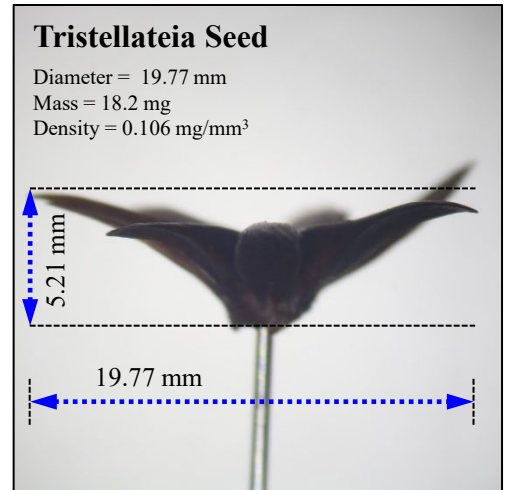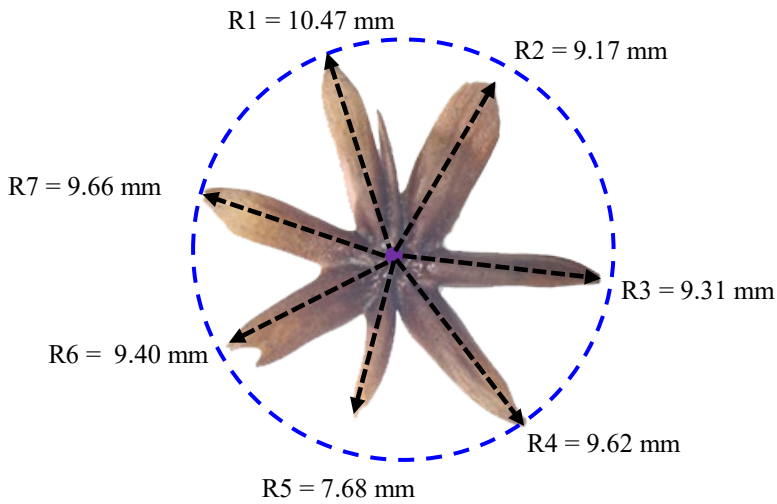**Supplementary information**

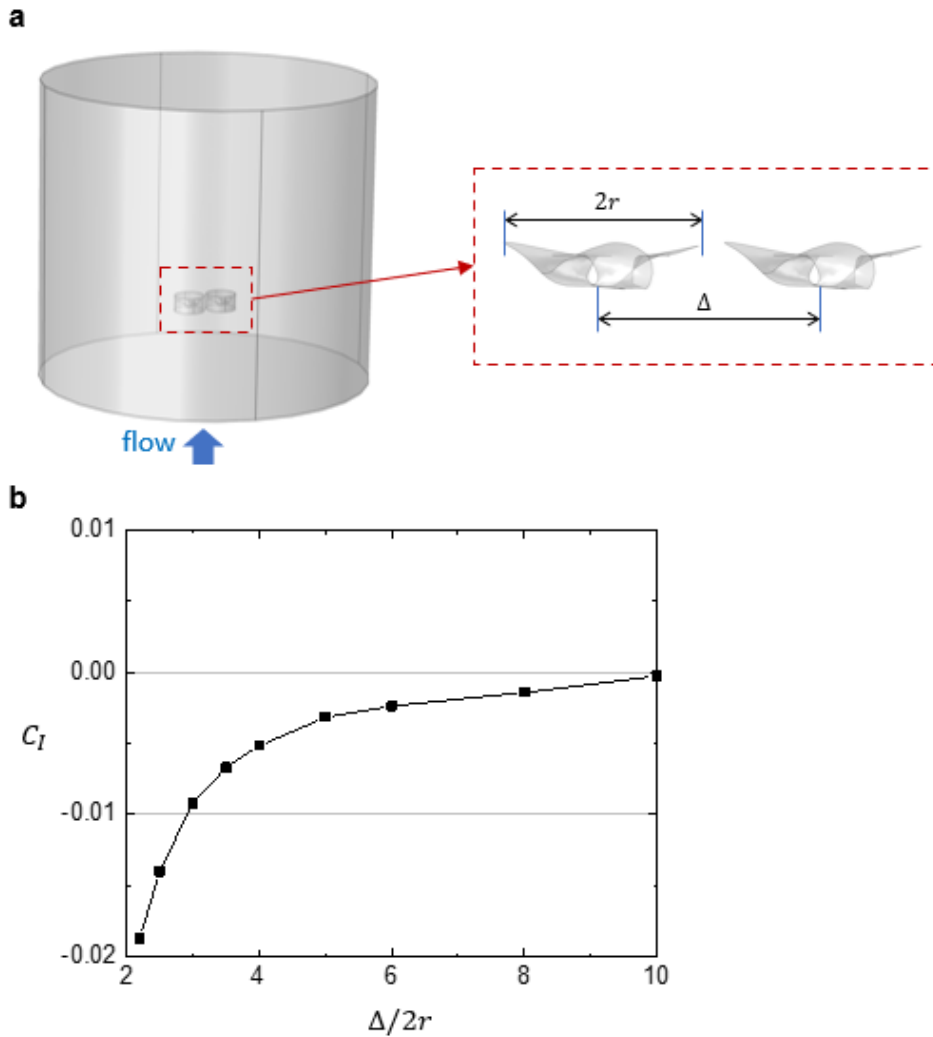# Three-dimensional electronic microfliers inspired by wind-dispersed seeds

In the format provided by the authors and unedited

Figure S1. A tristellateia seed. Optical images of a tristellateia seed from top and front views. The terminal velocity is ~100 cm/s.

Table S1. Mass of fliers at meso- and microscales.

Flier Designs	Meso- (d~2 mm)	Micro- (d~0.5 mm)
[2,R,0.2]	4.82 µg	0.301 µg
[2,H,0.6]	9.63 µg	0.602 µg
[2,H,1.2]	20.5 µg	1.28 µg
[3,H,0.6]	13.9 µg	0.872 µg
[3,H,0.75]	9.49 µg	0.593 µg
[3,M,0.4]	12.2 µg	0.763 µg
[3,PM,0.4]	9.16 µg	0.573 µg
[3,M,0.33]	11.5 µg	0.718 µg
[3,R,0.5]	6.73 µg	0.421 µg

a

b

Figure S2. Interaction forces between two mesofliers [3,M,0.4] falling in parallel at their terminal velocities ($Re\sim41$). (a) Schematic diagram of the falling mesofliers, with center-to-center distance Δ. (b) Normalized interaction force $C_I = F_I/(0.5\rho v_T^2 A)$ versus the normalized distance $\Delta/2r$, with F_I denotes the interaction force.
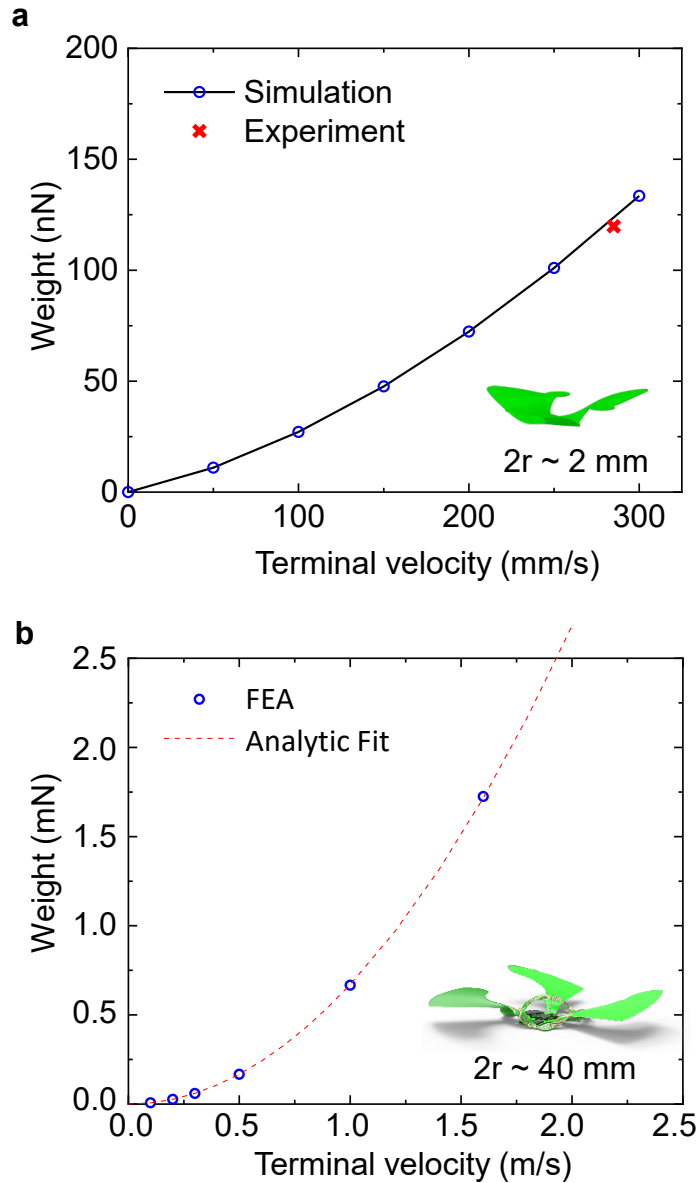
Figure S3. Relation between flier weight and terminal falling velocity. (a) Plot that indicates a nearly linear relationship between weight and terminal velocity for a mesoflier with small Reynolds number (Re~40). (b) Plot that indicates an approximately parabolic relationship between weight and terminal velocity for a macroflier with large Reynolds number (Re~3000).

a

b
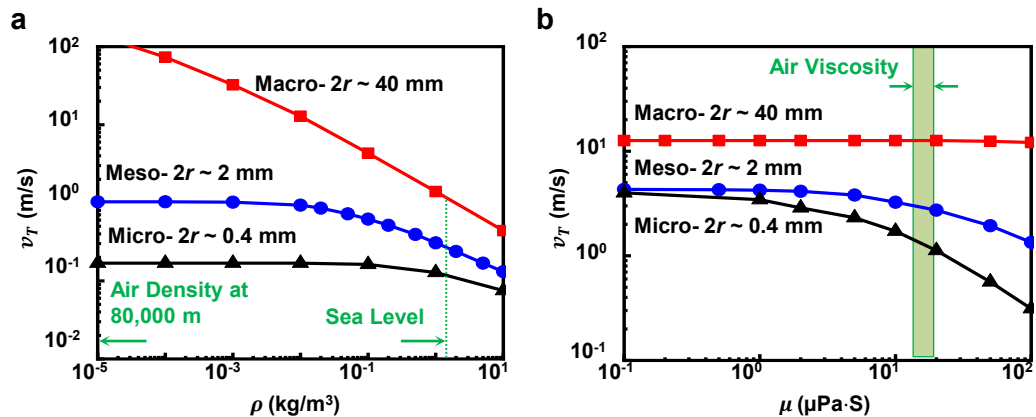
Figure S4. Effect of air properties. Dependence of terminal velocity on (a) the density and (b) the dynamic viscosity of air for multi-scale fliers. The behavior of the macrofliers depend mainly on the density; the behaviors of the meso- and microfliers depend mainly on the dynamic viscosity.
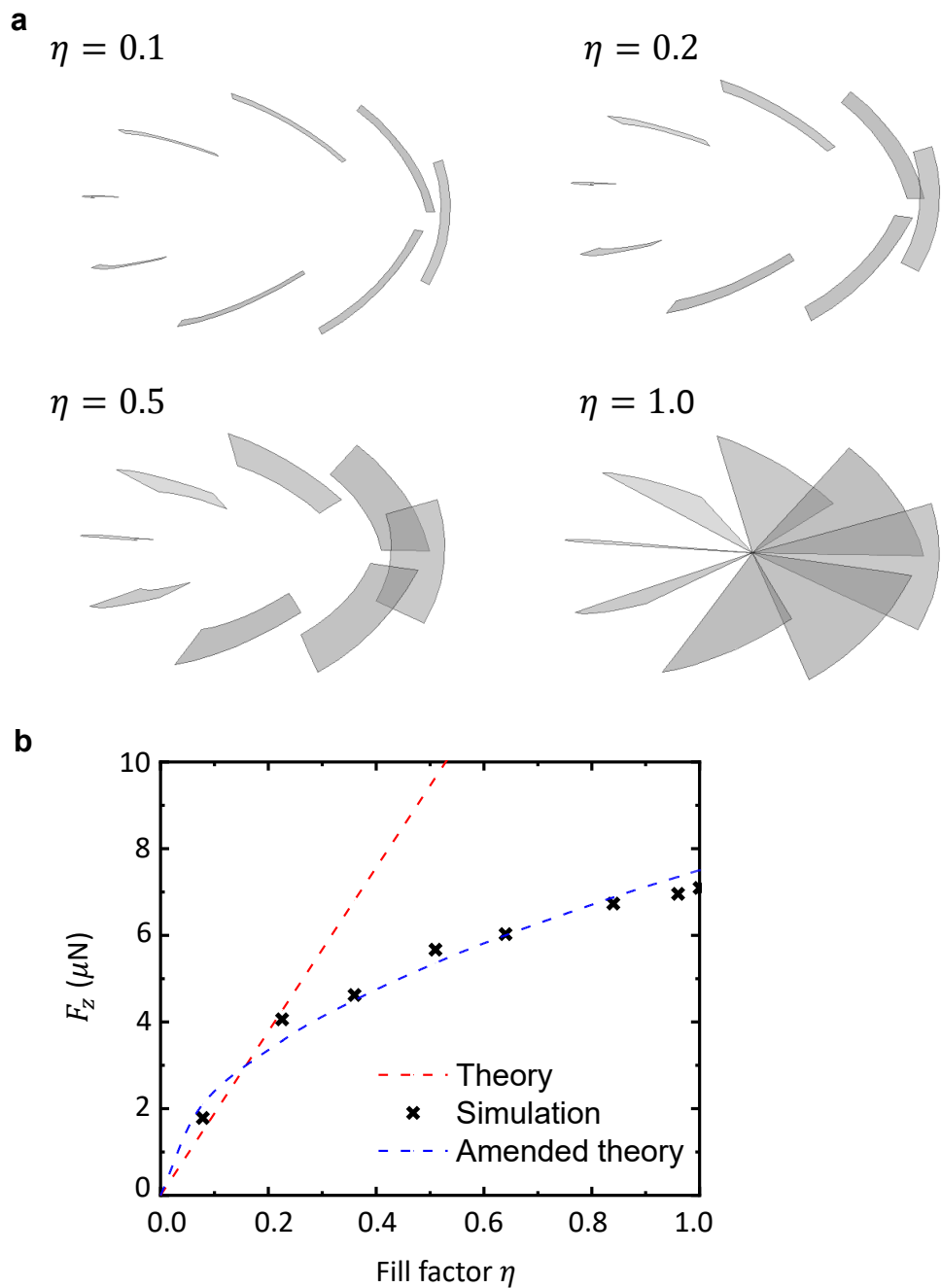
Figure S5. Amended dependence of the vertical-direction drag force of a 3D mesoflier on the fill factor at small Reynolds number (Re~40). (a) Schematic diagram of the simplified mesoflier model with various fill factors. (b) Weight to terminal velocity ratio versus fill factor for a mesoflier at small Reynolds number. The results follow from the fitting law $F_z \propto \sqrt{\eta}$.
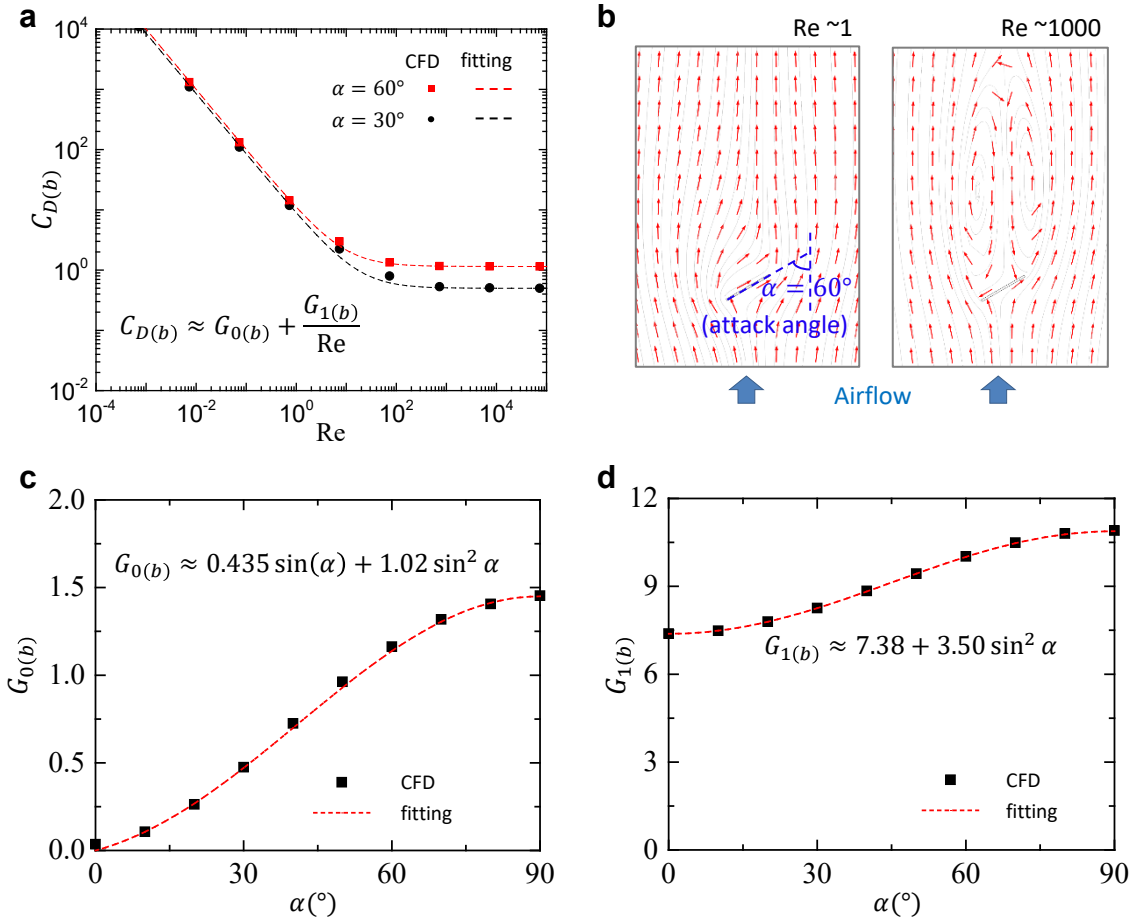
Figure S6. Aerodynamic properties of 2D flat airfoil (cross-section of blade) for various attack angles. (a) Drag coefficient of the 2D airfoil versus the Reynolds number. CFD results are fitted by $C_{D(b)} \approx G_{0(b)} + \frac{G_{1(b)}}{\text{Re}}$, that $(G_{0(b)}, G_{1(b)}) = (0.50, 8.3)$ for $\alpha = 30°$ and $(G_{0(b)}, G_{1(b)}) = (1.15, 10)$ for $\alpha = 60°$. (b) Stream and quiver plot for the flow field around a flat airfoil of attack angle $\alpha = 60^o$, for Re ~ 1 and 1000, respectively. CFD results of (c) $G_{0(b)}$ and (d) $G_{1(b)}$ of the 2D airfoil versus the attack angle, as analytically fitted by $G_{0(b)} \approx 0.435 \sin(\alpha) + 1.02 \sin^2 \alpha$ and $G_{1(b)} \approx 7.38 + 3.50 \sin^2 \alpha$, respectively.
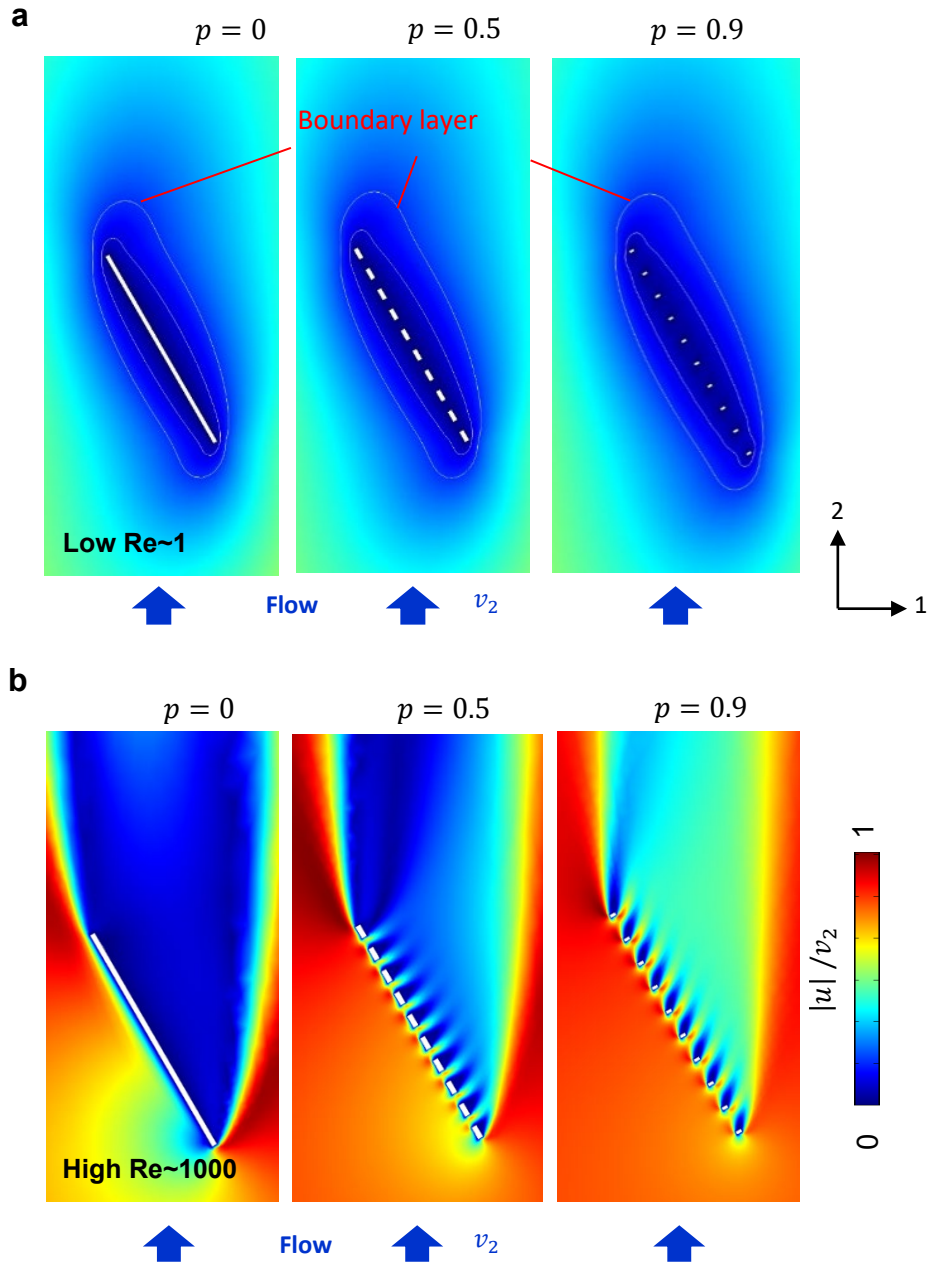
Figure S7. Velocity fields for airfoil with 3 different porosities (p=0, 0.5 and 0.9). (a) low Re and (b) high Re. The boundary layers at low Re are shown by velocity contours at $|u|/v_2 = 0.1$. At low Re, the boundary layer surrounding the airfoil, which can be seen as a virtual airfoil, is not affected by the porosity on the flat airfoil. The drag force acting on the airfoil is therefore not significantly decreased.
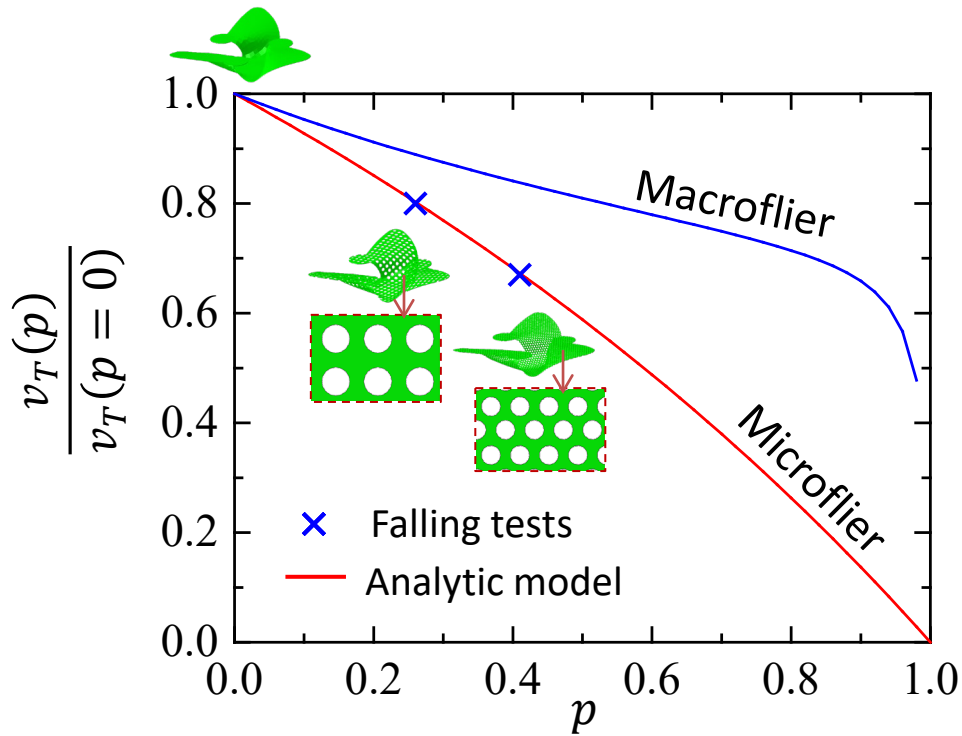
Figure S8. Terminal velocity versus porosity (p) for micro- and macrofliers. The terminal velocity for the microflier is validated by experimental falling tests (Fig. 3b). Porosity design is more effective on microfliers than on macrofliers.

a

$c/r_0 = 0$ (flat)

$c/r_0 = 0.50$

$c/r_0 = 0.67$

$c/r_0 = 1.0$

r_0

c

b

c
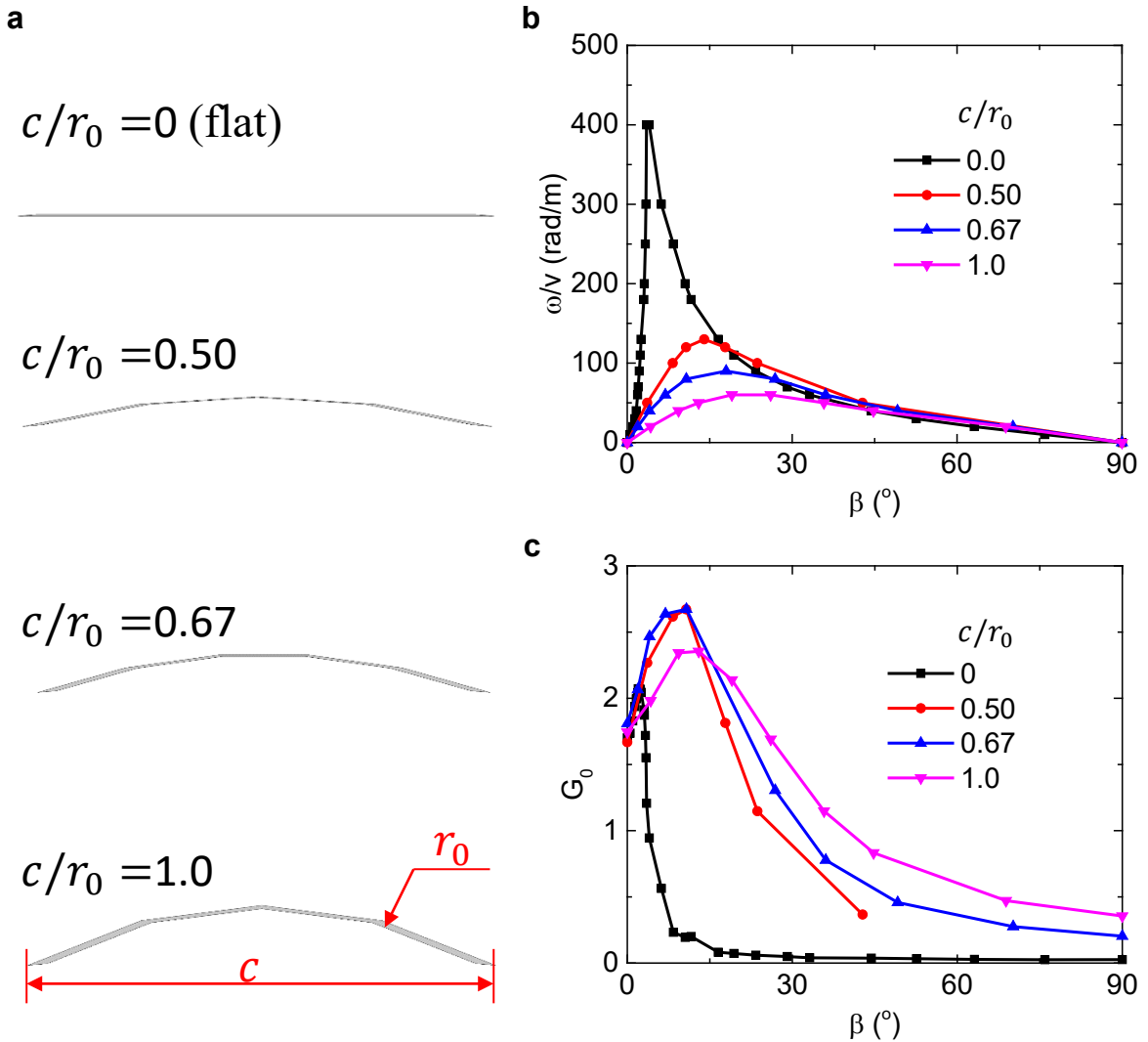
Figure S9. Effect of airfoil curvature for fliers at high Reynolds numbers. (a) Scheme for airfoils (cross section of a blade) with different curvatures. (b) ω/v_T and (c) G_0 versus blade tilt angle with different airfoil curvatures (from flat to curved), at high Re ~3000. With curvature $c/r_0 = 0.5$, G_0 can be increased by ~35% compared to the flat blade.

a

$\beta = 0°$

$\beta = 30°$

$\beta = 60°$

$\beta = 90°$

b

c
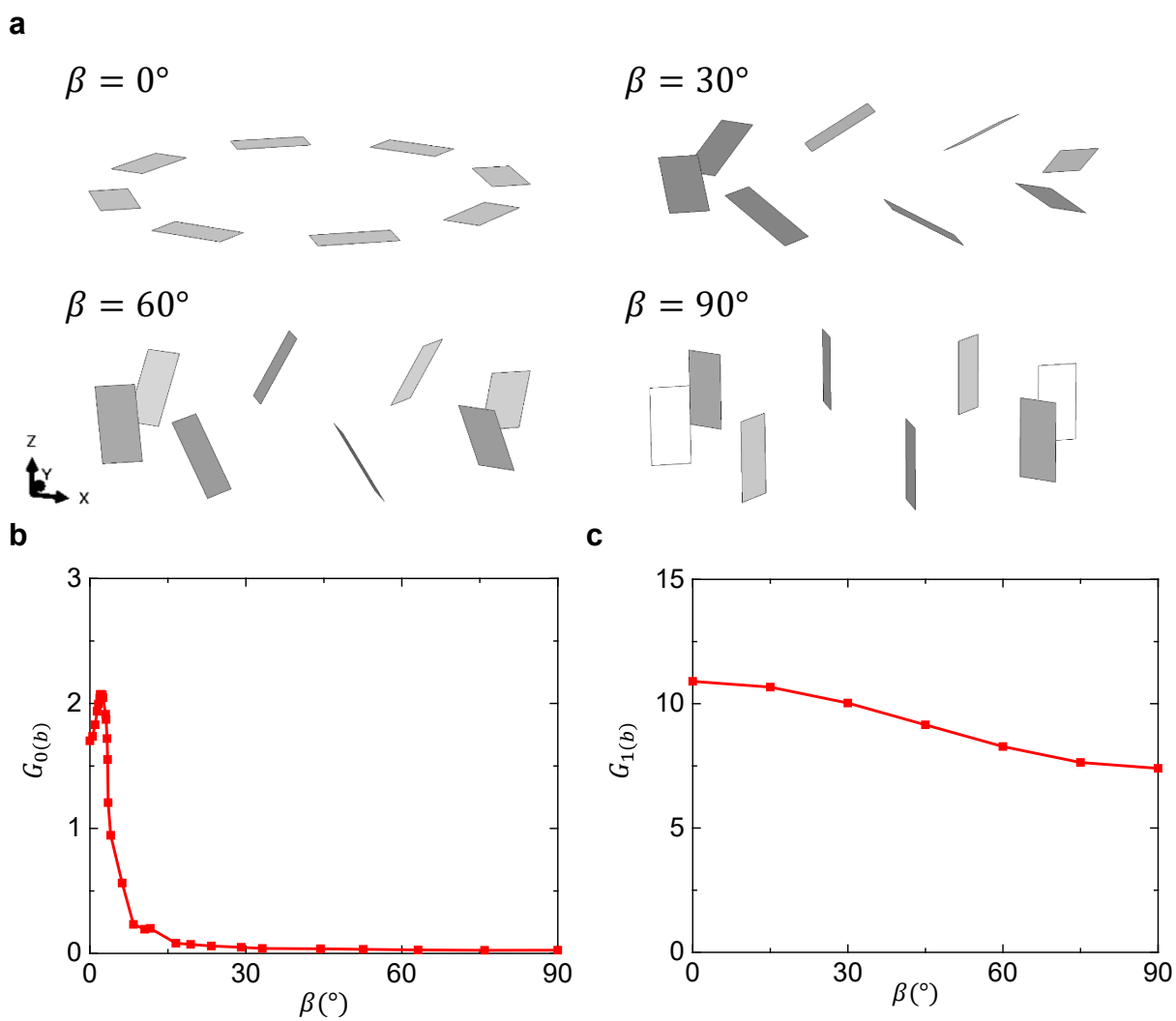
Figure S10. Effect of tilt angles of blades on G_0 and G_1. (a) Scheme of the simplified flier model with different tilt angles (β). The effect of tilt angle on (b) G_0 and (c) G_1. Optimizing the tilt angle (rotational behavior) will slightly increase G_0, but decrease G_1.
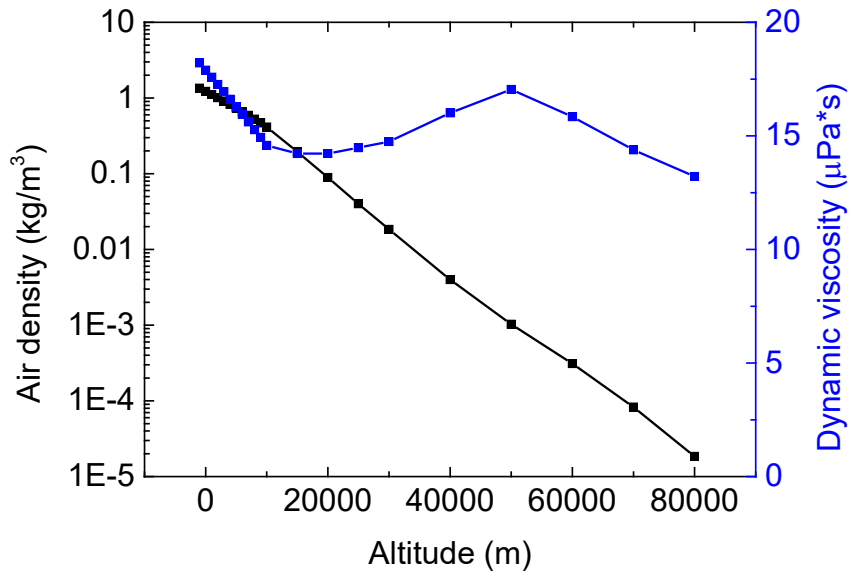
Figure S11. Effect of air properties. Air properties (density and dynamic viscosity) of US standard atmosphere at altitudes ranging from 0 to 80,000 m.
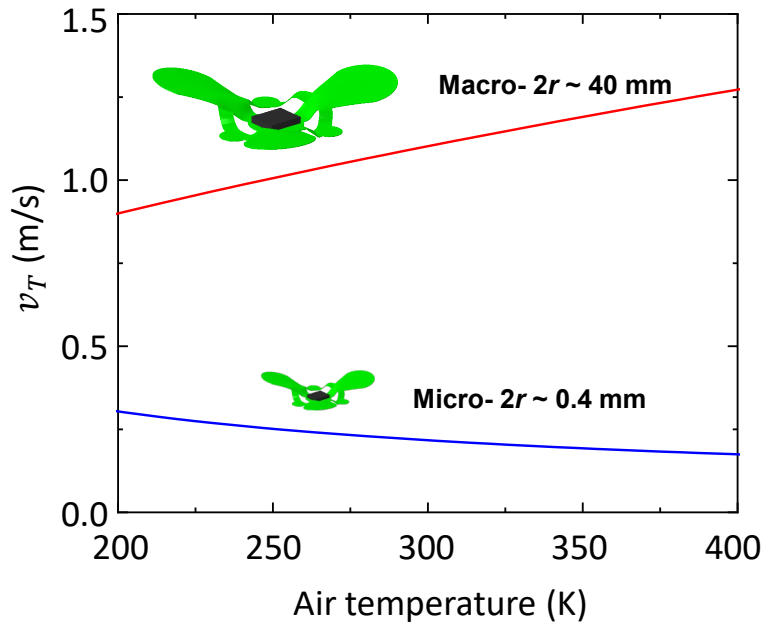
Figure S12. Effect of air properties. Effect of air temperature on terminal velocity. The terminal velocity of macro- and microfliers follow from different dependence on the air temperature, because μ increases but ρ decreases with temperature increasing.
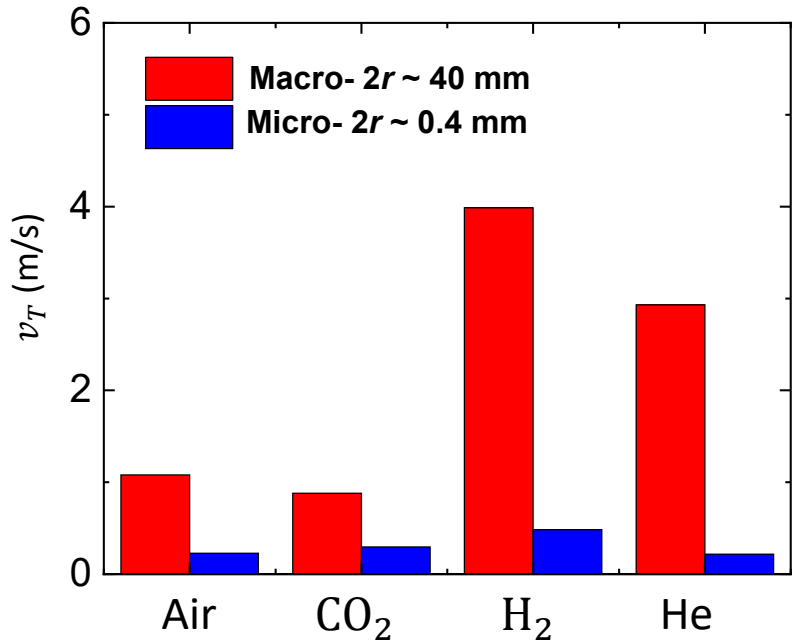
Figure S13. Effect of molecular makeup. CFD simulations for small and large fliers falling in different gases. The different μ and ρ indicate macro- and microfliers show a different dependence on molecular makeup of the gas. For example, In He, the microflier has the smallest v_T among all gases, but macroflier falls quickly in this same environment.
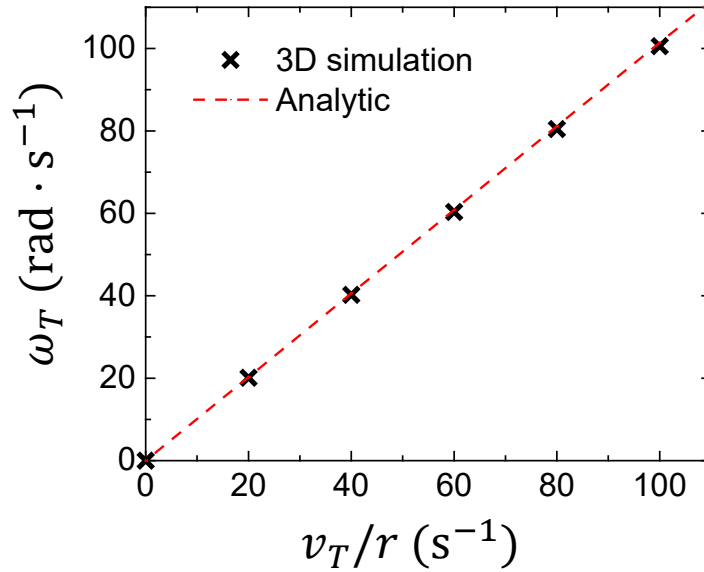
Figure S14. Scaling law for the terminal rotating speed of a flier. The rotating speed ω_T versus v_T/r, and the CFD results show a linear relationship, consistent with the analytic model $\dfrac{\omega_T r}{v_T} = \dfrac{C_{L(b)}}{C_{D(b)}} = L_D$.
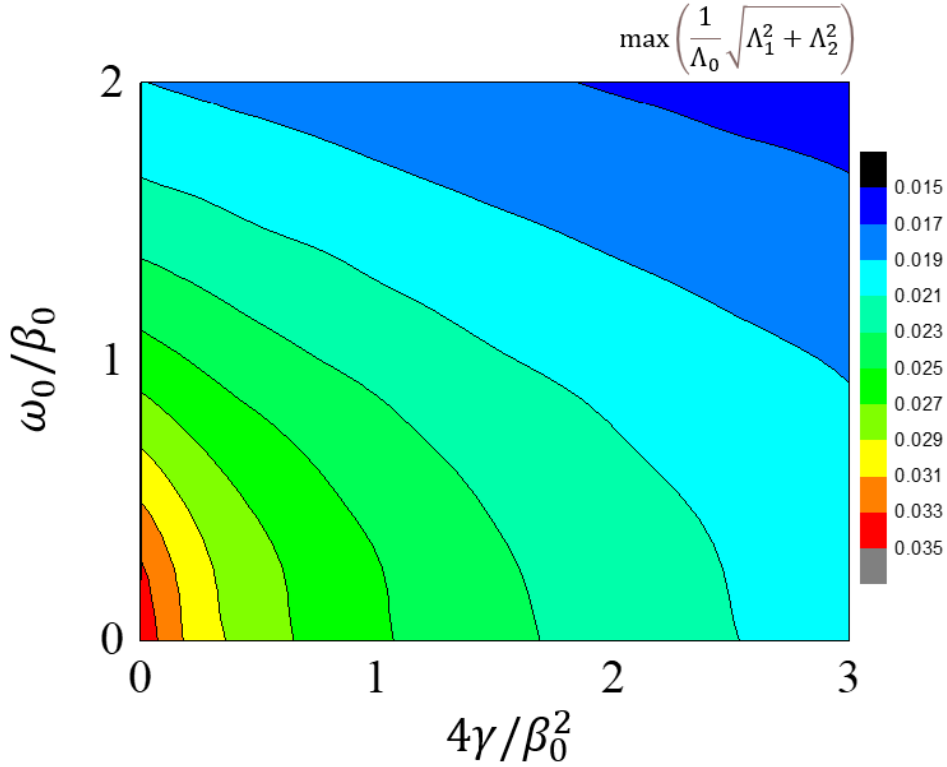
Figure S15. Maximum perturbed angle. The maximum perturbed angle $\max\left(\frac{1}{\Lambda_0}\sqrt{\Lambda_1^2 + \Lambda_2^2}\right)$ versus ω_0/β_0 and $4\gamma/\beta_0^2$, where $\beta_0 = \frac{\pi}{8}\frac{\mu r^2}{\sqrt{\eta}} \cdot \text{Re}\left(2G_0 + \frac{G_1}{\text{Re}}\right)\frac{1}{I_1}$, $\omega_0 = \frac{I_3-I_2}{I_1}\omega_T$, $\gamma = \frac{Wd}{I_1}$, $I_{1,2,3}$ are the moment of inertias for directions 1, 2 and 3, and d is the distance between the center of gravity and the center of pressure. Rotation with higher $\omega_0 \propto \omega_T$ will lead to lower $\max\left(\frac{1}{\Lambda_0}\sqrt{\Lambda_1^2 + \Lambda_2^2}\right)$, indicating the rotational stability.
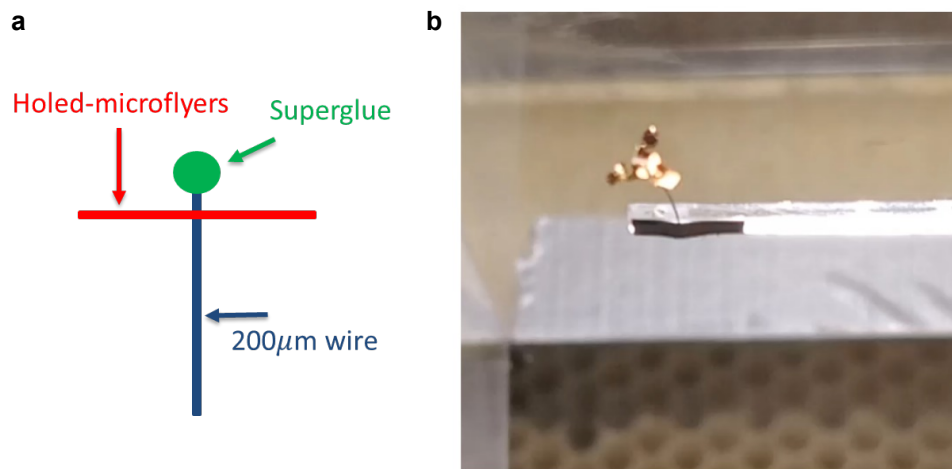
Figure S16. A fixed 3D macroflier above a wind tunnel. (a) Schematic diagram of a fixed macroflier, (b) video of comparing 2D (non-rotating) and 3D (rotating) macrofliers with $r = 1.7$ mm.
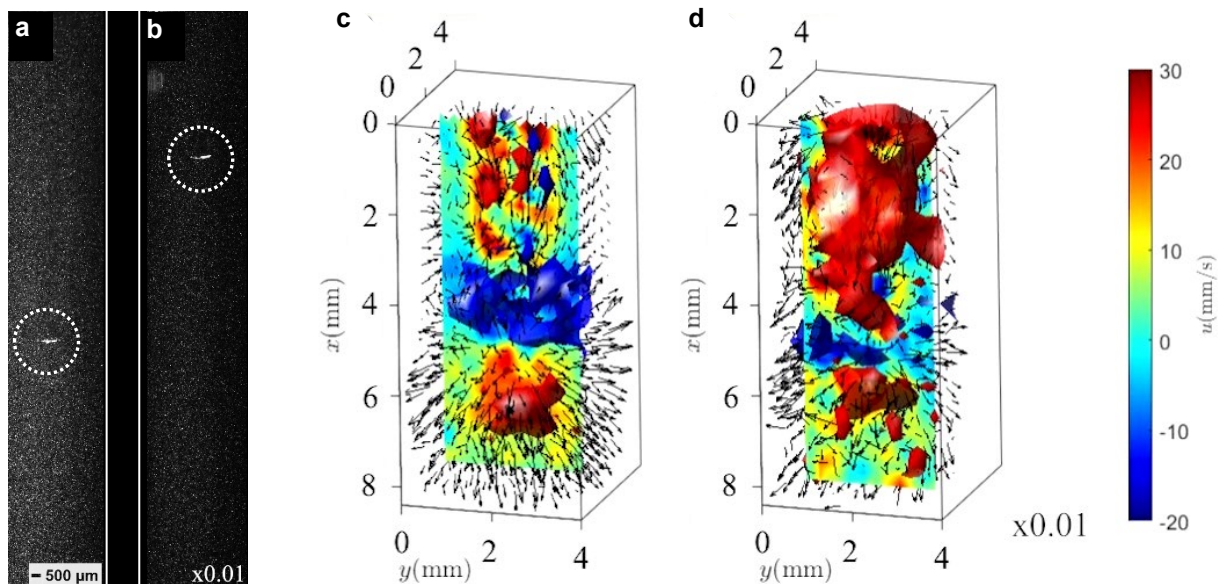
Figure S17. Free-falling 2D precursor and 3D mesoflier. (a) Free-falling 2D precursor, (b) Free-falling 3D mesoflier. Instantaneous 3D flow velocity fields induced by free-falling (c) 2D precursor and (b) 3D mesoflier measured via 3D-PTV. The color denotes the in-plane 2D vertical velocity along the flier's center plane. Red and blue-sio-surfaces demonstrate iso-values of 15 and -5 mm/s, respectively. The rotational dynamics of the 3D mesofliers minimize flow separation and induce large momentum deficits, resulting in stable and slow falling behaviors.

a 2D Precursor

b 3D Mesoflier

u (mm/s)

-30

-20
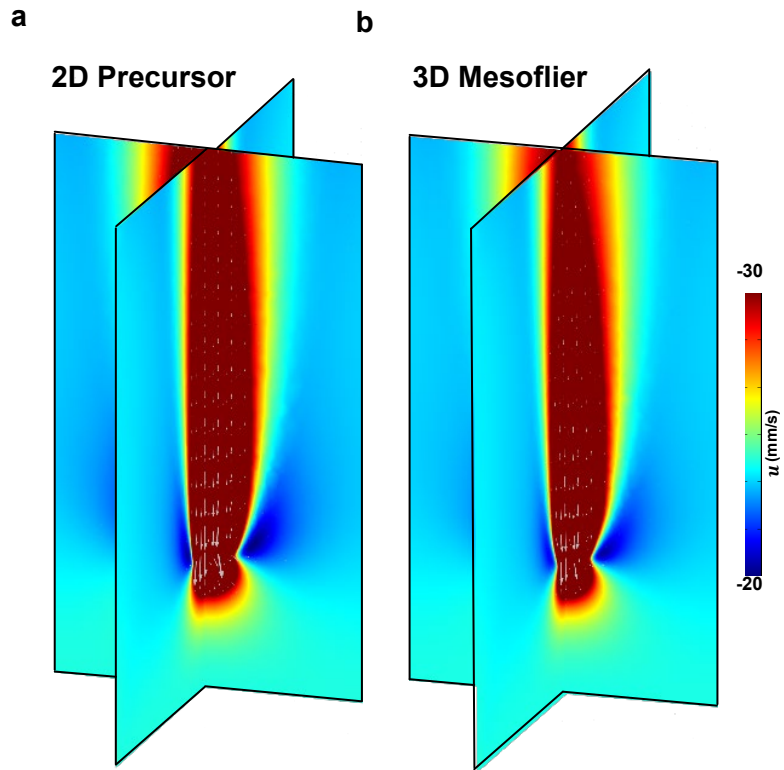
Figure S18. CFD simulated vertical flow field. (a) A 2D precursor and (b) 3D mesoflier [3,M,0.4] (Size scale 2r ~ 2 mm). The simulation agrees well with the experimentally measured flow field.
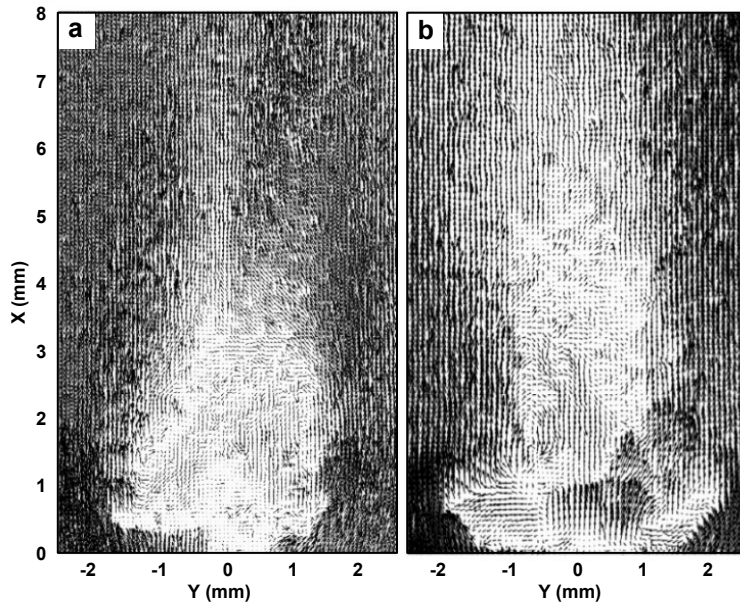
Figure S19. Experimental results for mesoflier. Instantaneous velocity fields induced by a fixed (a) 2D precursor and (b) 3D mesoflier *via* PIV above the wind tunnel. Flow fields induced by the 3D mesoflier exhibit a larger momentum deficit than the 2D precursor.

Table S2. Types of possible electronic components and wireless systems integrated on 3D meso- and macro-fliers.

Types and # of possible electronic components integrated on 3D mesoflier	Silicon CMOS 5×10^9 transistors	Solid-State Memory 10^{11} bits	Solar Cell 4 units	Miniature Lasers 10^6 units	mm-scale Computer 4 units

Types of possible wireless systems integrated on 3D IoT macroflier	Near-Field Communication (NFC)	Bluetooth Low Energy (BLE)	Radio-Frequency Identification (RFID)	Optical Technology (colorimetric readout)
Effective Distance	~ 1 m	~100 m	~2 m (chipless tag) ~5 m (passive tag) ~ 100 m (active tag) ~10 km (very high frequency tag)	A range of tens of km's
The Size of Miniaturized Antenna	5-10 mm	1-2 mm	10~50 mm	N/A

a

2D Precursor

b

3D Mesoflier

c

$w\,(\mathrm{nm})$

52

0

d

0.38 m/s

20.5 µg

v_T (m/s)

Mass (µg)
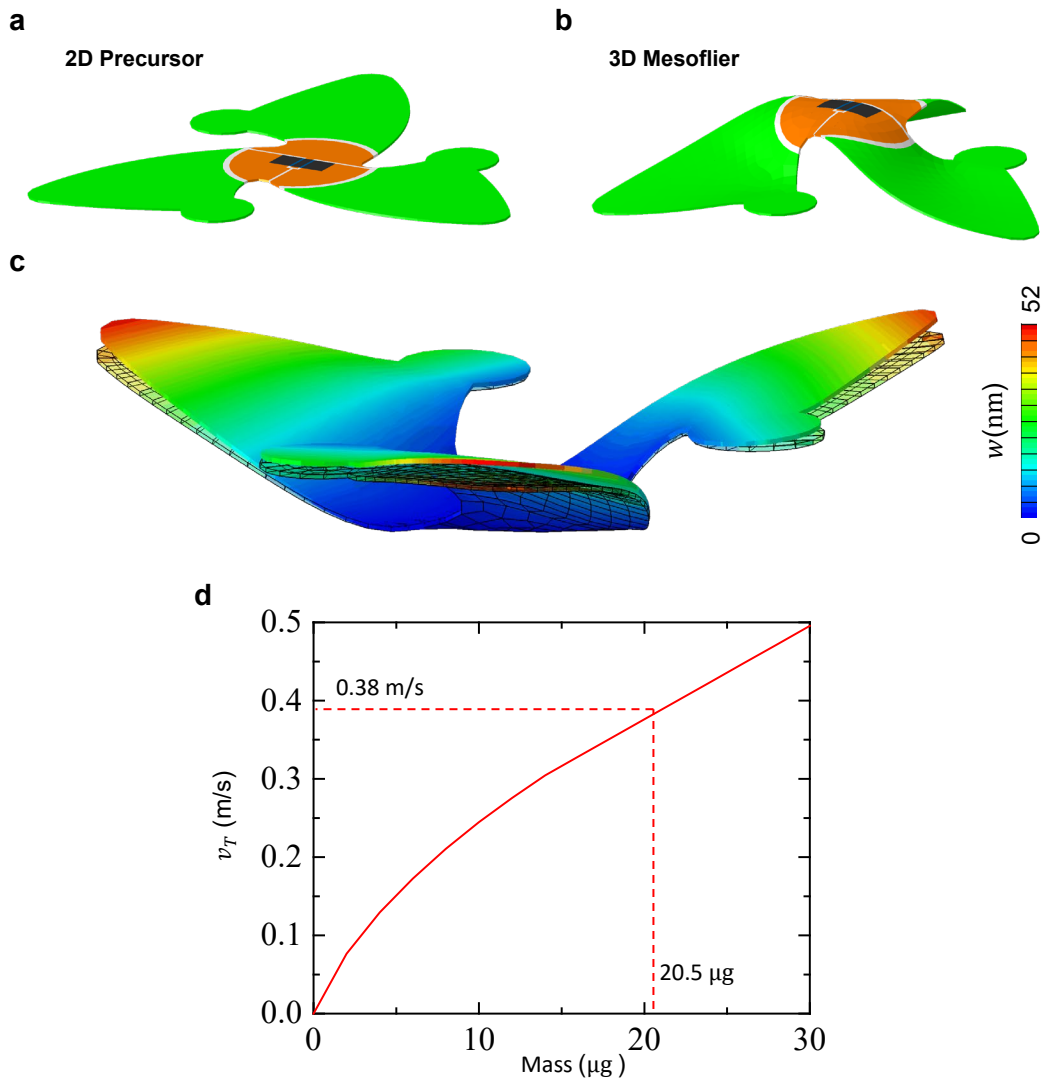
Figure S20. Simulations for 3D mesoflier design I [3,M,0.4]. FEA showing (a) 2D precursor and (b) 3D configuration for the mesoflier. (c) Deflection of the 3D mesoflier during free-fall at the terminal velocity. The deflection is magnified by 1000 times. (d) CFD results for the terminal velocity as a function of the mass of the mesoflier. The deflection of the mesoflier during free fall at the terminal velocity has only a slight effect on its 3D configuration.

a

2D Precursor

b

3D Mesoflier

c

w(nm)

35

0

d

0.32 m/s

16.5 μg

v_T (m/s)

Mass (μg)
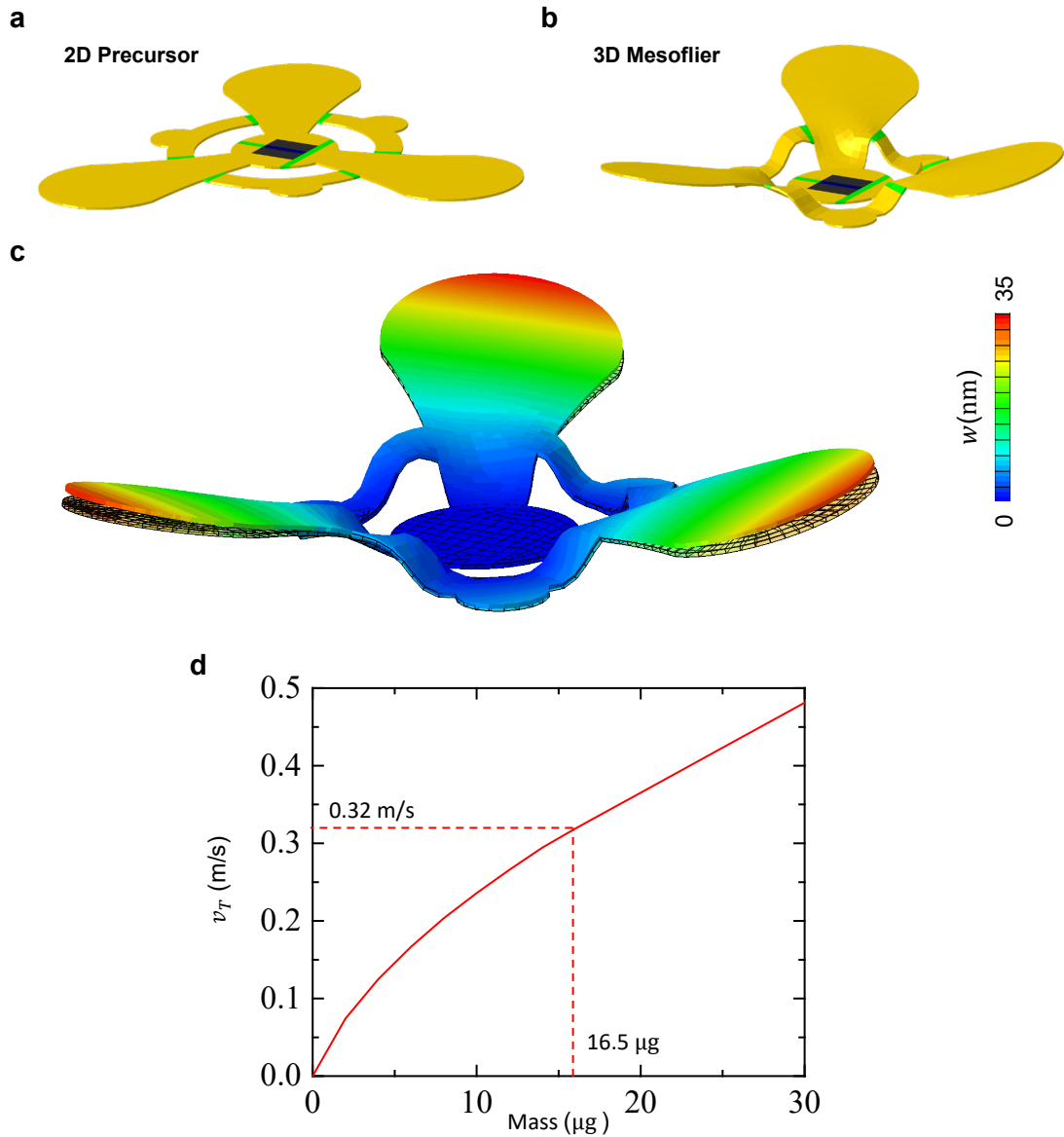
Figure S21. Simulations for 3D mesofliers with design II [3,H,0.75]. FEA showing (a) 2D precursor and (b) 3D configuration for the mesoflier. (c) Deflection of during free-falling at the terminal velocity. The deflection is magnified by 1000 times. (d) CFD results for the terminal velocity as a function of the mass of the mesoflier.
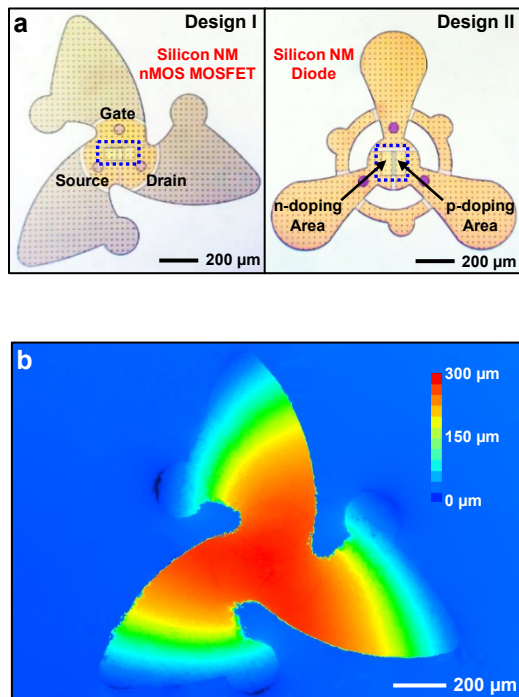
Figure S22. 3D electronic mesofliers. **a,** optical micrographs of 2D precursors for 3D electronic mesofliers [3,M,0.4] and [3,H,0.75] with Si NM nMOS transistors and diodes as payloads. **b,** 3D surface profile of a 3D mesoflier [3,M,0.4].
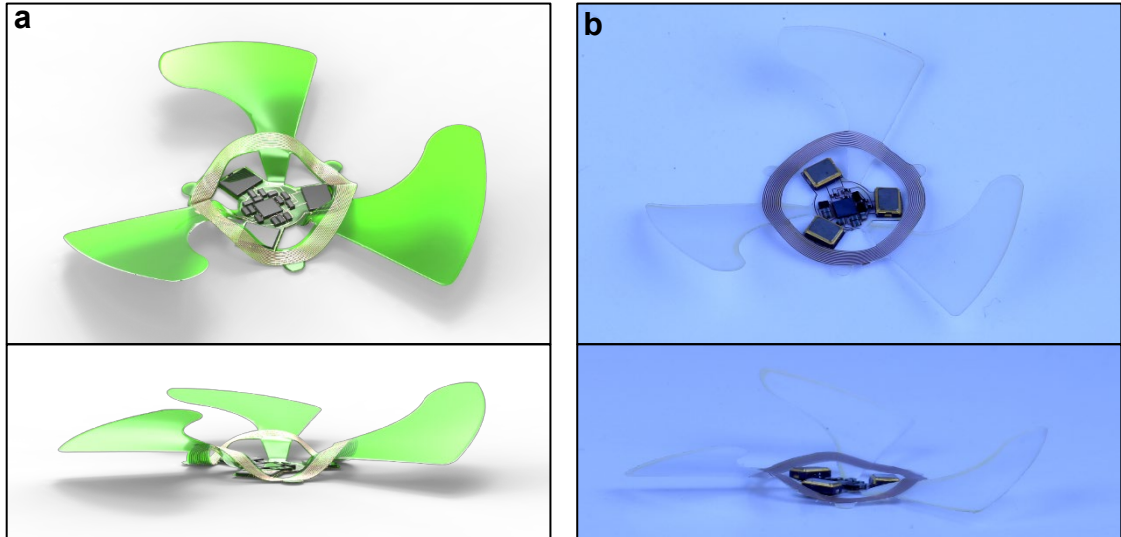
Figure S23. A 3D IoT macroflier with another design. (a) Mechanical simulation results and (b) photographs with a circuit to measure fine dust pollution through the light dosimetry method. The mechanical simulation guides the design and well predicts the fabricated configuration of the IoT macroflier. The weight of this flier is 14.6 mg (d~4cm), with payload 75.4mg.
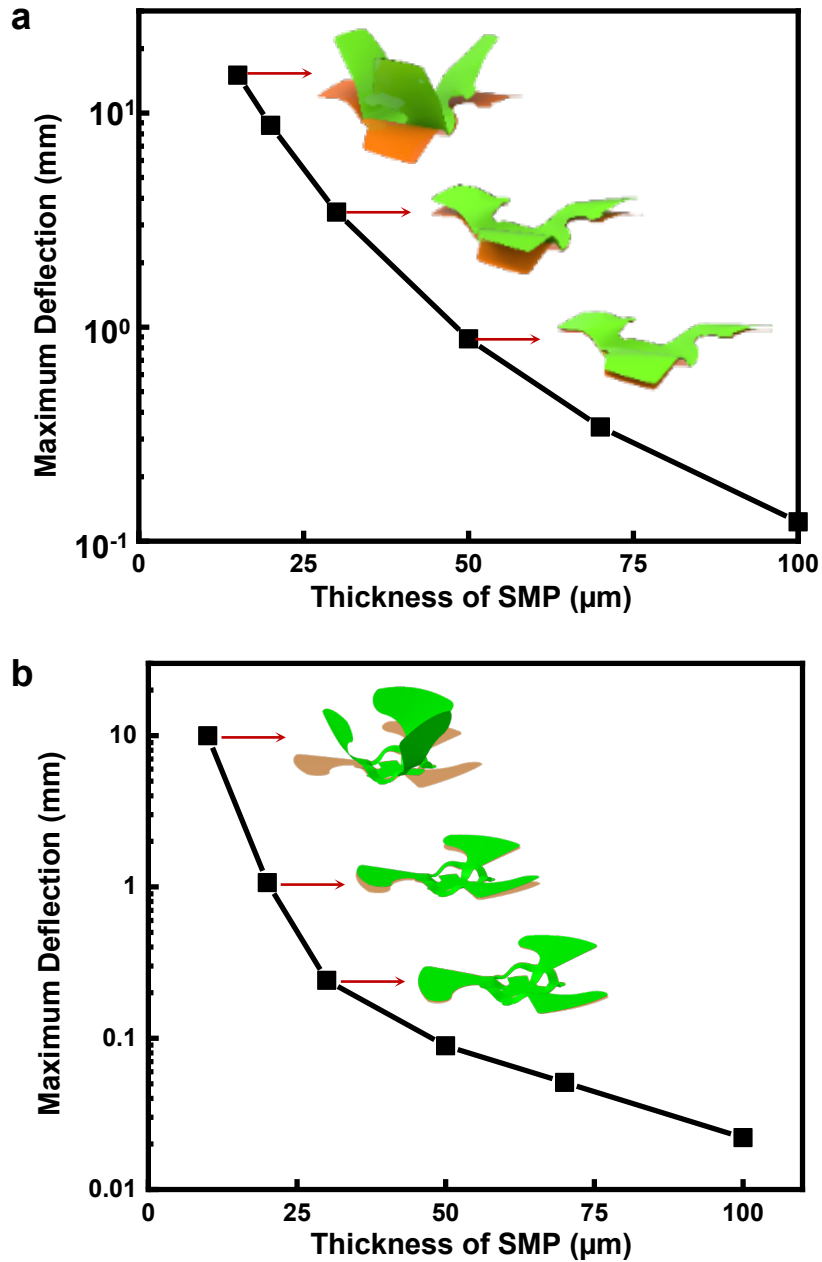
Figure S24. Effect of thickness on the deflection of 3D IoT macrofliers during falling. 3D IoT macrofliers with (a) IoT design I and (b) IoT design II, respectively. A thick SMP layer >12 μm can limit the deflection of the structure to <2 mm for IoT fliers (2r ~ 20 mm) during falling.

a

2D NFC Coil

3D NFC Coil

b

2D NFC Coil

3D NFC Coil
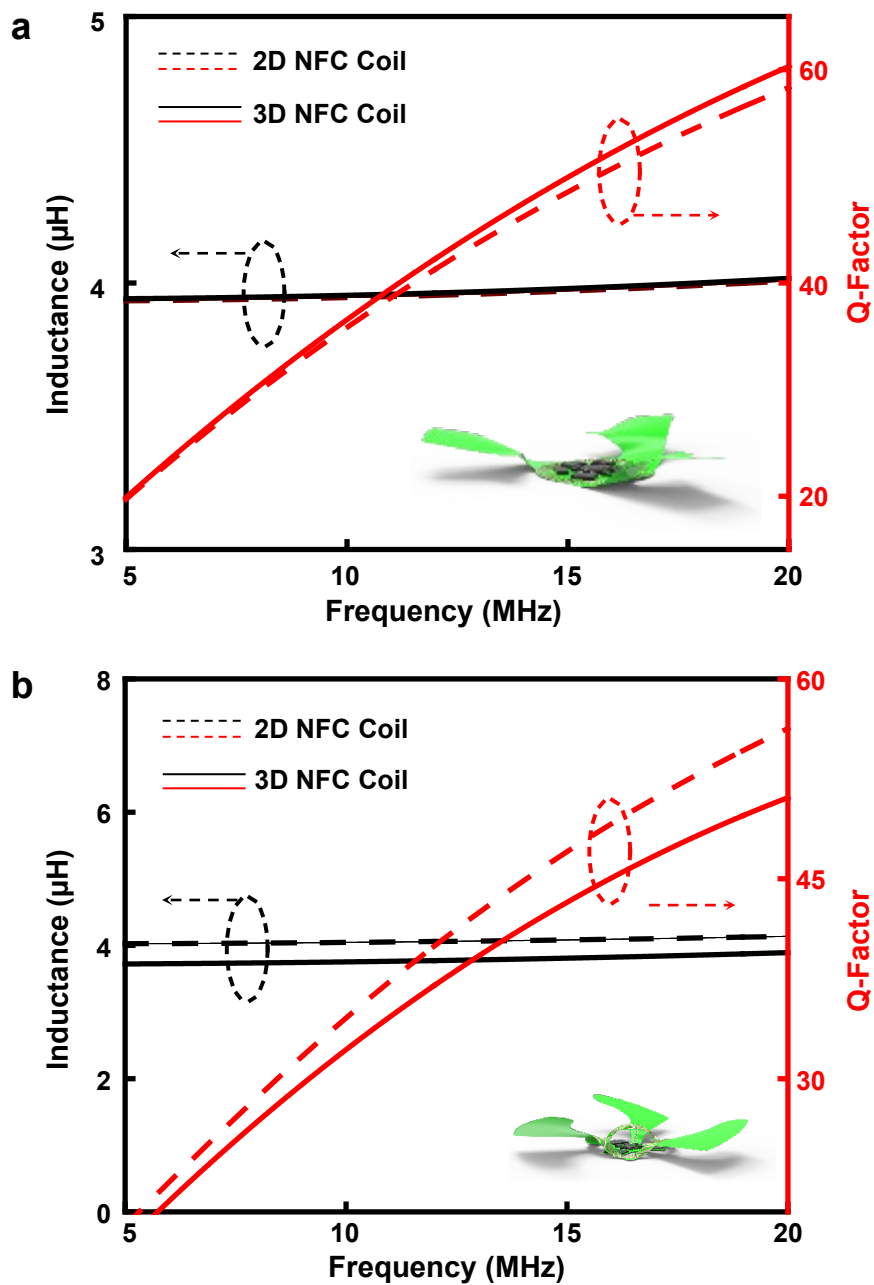
Figure S25. Electromagnetic simulations. Inductance and Q-factor for 3D IoT macrofliers with (a) IoT design I and (b) IoT design II for 2D/3D configuration, respectively. Electromagnetic simulations guide the designs of the antennas and prove the feasibility.
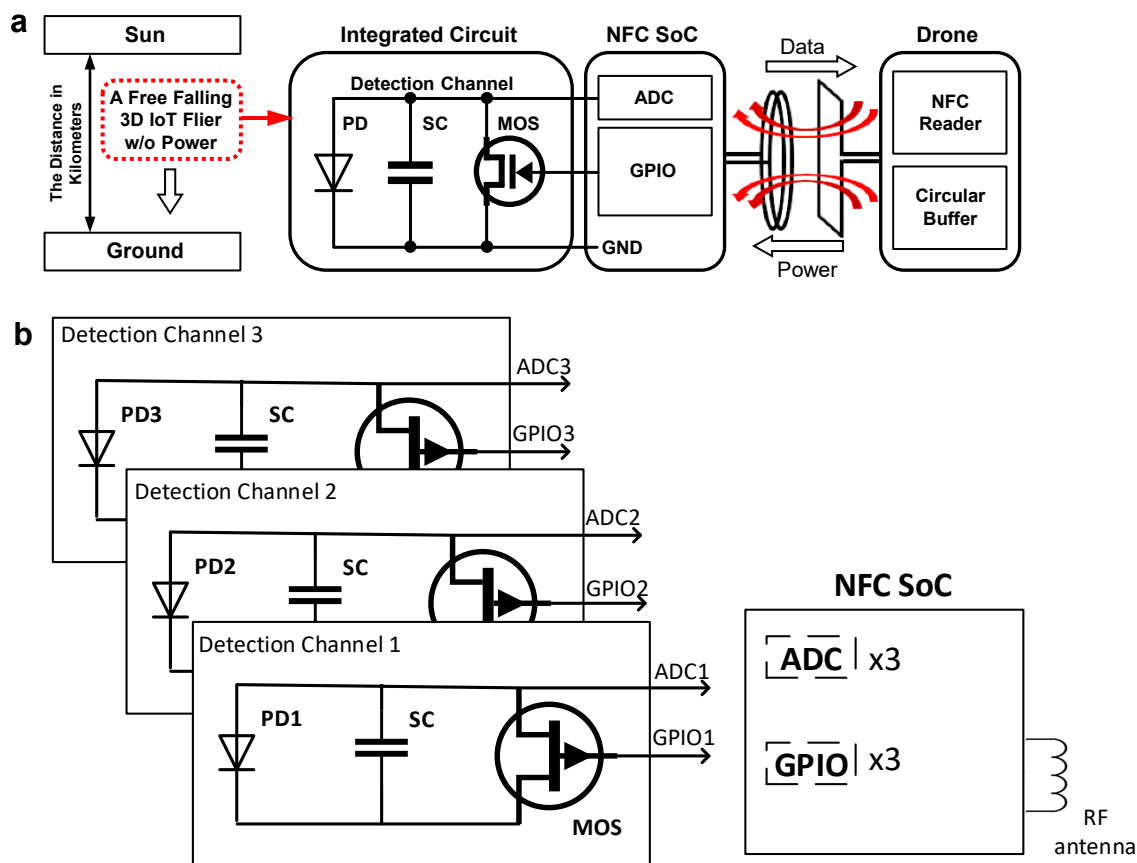
Figure S26. Circuit schematic of a battery-free, 3-channel dosimeter for fine dust monitoring. (a) A 3D IoT macroflier and its wireless interface to a drone. (b) Each detection channel consists of a photodiode (PD), a supercapacitor (SC), and a MOSFET (MOS). Upon light exposure, PD continuously generates photocurrent and SC passively stores the accumulated charge. The voltage bias of the SC read via ADC is proportional to the total exposure dose. Simultaneous dosimetry at up to three different wavelengths are possible by PD selection. An Near Field Communication System on Chip (NFC SoC) allows for a battery-free and wireless data transfer and power transmission. Wirelessly activated GPIO supplies 1.5V to the gate of the MOS and triggers SC discharge.
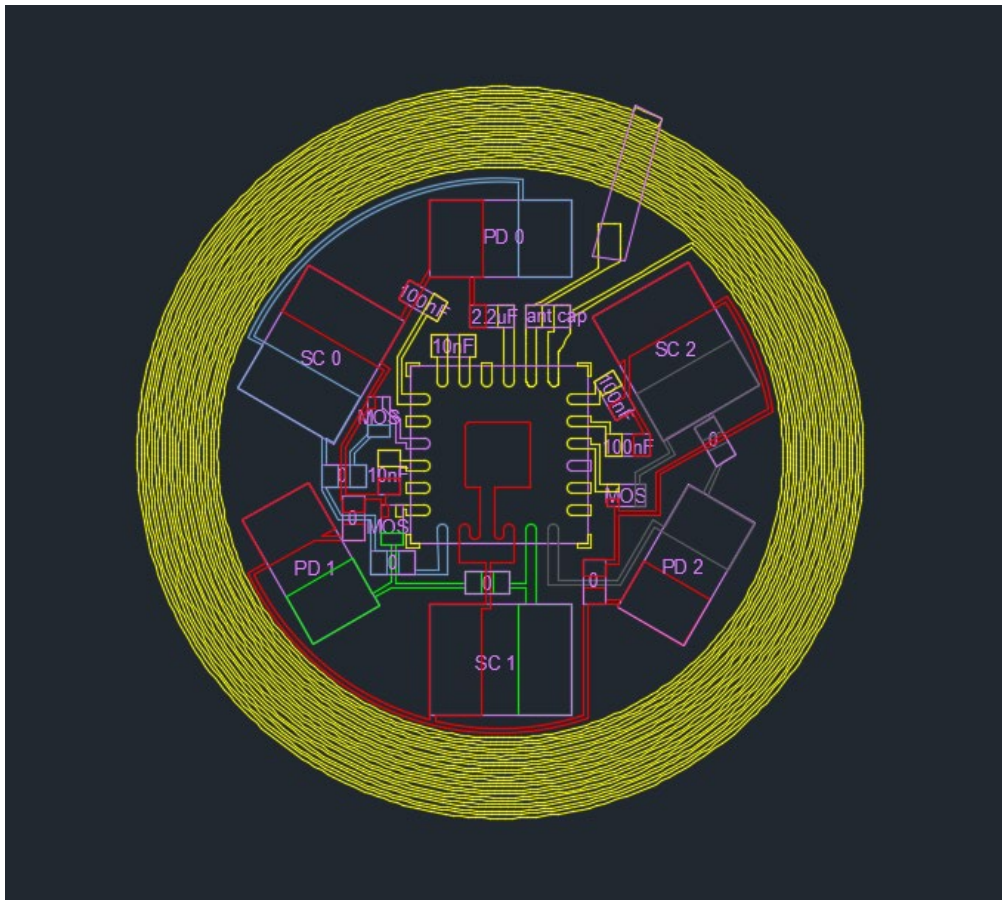
Figure S27. CAD design. Electronic components and metal interconnectors for a 3D IoT macroflier.

Table S3. Electronic components. The list of a detailed information of electronic circuits for a battery-free, 3-channel dosimeter for fine dust monitoring.

Item	Manufacturer	Catalog Number	Description
NFC Chip	Texas Instruments	RF430FRL152HC RGER	RFID Transponders Sensor Transponder
Photodiode	Advanced Photonix	PDB-CD160SM	Photodiode 850nm 20ns 120° 2-SMD, Gull Wing
MOSFET	Texas Instruments	CSD17381F4	MOSFET N-CH 30V 3.1A 0402
Super-Capacitor	Seiko Instruments	CPH3225A	CAP 11MF 3.3V SURFACE MOUNT
Capacitor 1	Murata Electronics North America	GRM033R60J22 5ME47D	CAP CER 2.2UF 6.3V X5R 0201
Capacitor 2	TDK Corporation	C0603X7R1A103 K030BA	CAP CER 10000PF 10V X7R 0201
Capacitor 3	TDK Corporation	C0603X5R1A104 K030BC	CAP CER 0.1UF 10V X5R 0201
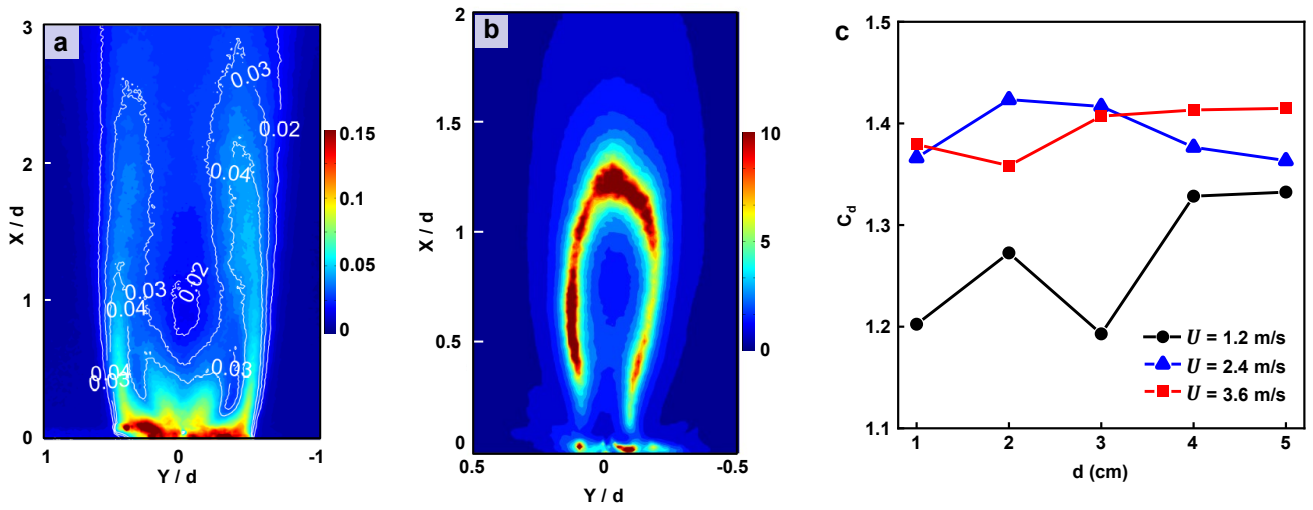
Figure S28. High-speed PIV measurements for 3D macrofliers. (a) turbulent Kinetic energy $TKE = \frac{1}{2}\left[\overline{(u')^2} + \overline{(v')^2}\right]/U^2$. (b) turbulence intensity $TI = \sqrt{\overline{(u')^2} + \overline{(v')^2}}/\sqrt{\bar{u}^2 + \bar{v}^2}$. (c) drag coefficient, C_d, calculated from velocity profiles vs diameters, d.
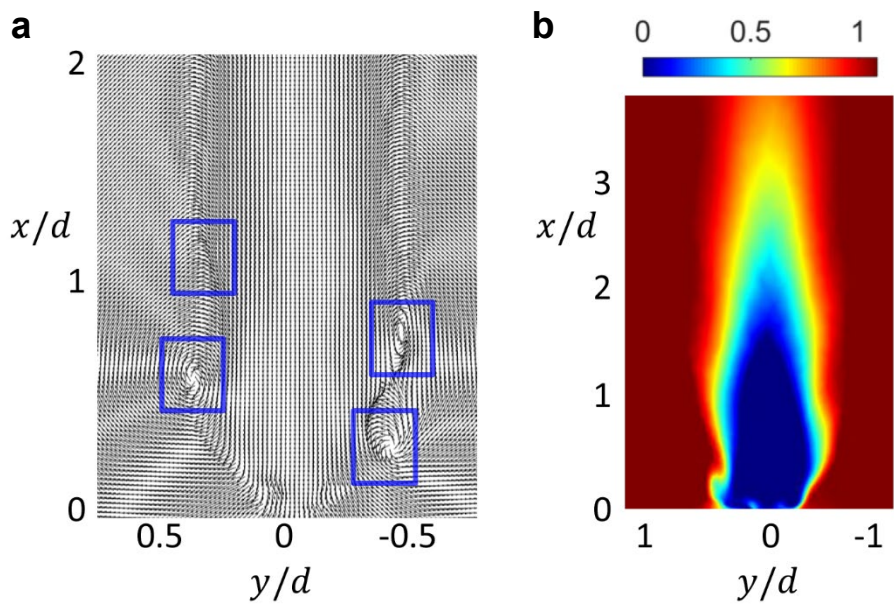
Figure S29. CFD results for a 3D IoT macroflier. (a) Instantaneous velocity field. (b) Mean velocity field in the streamwise direction u/U. The CFD simulation agrees well with the PIV results.
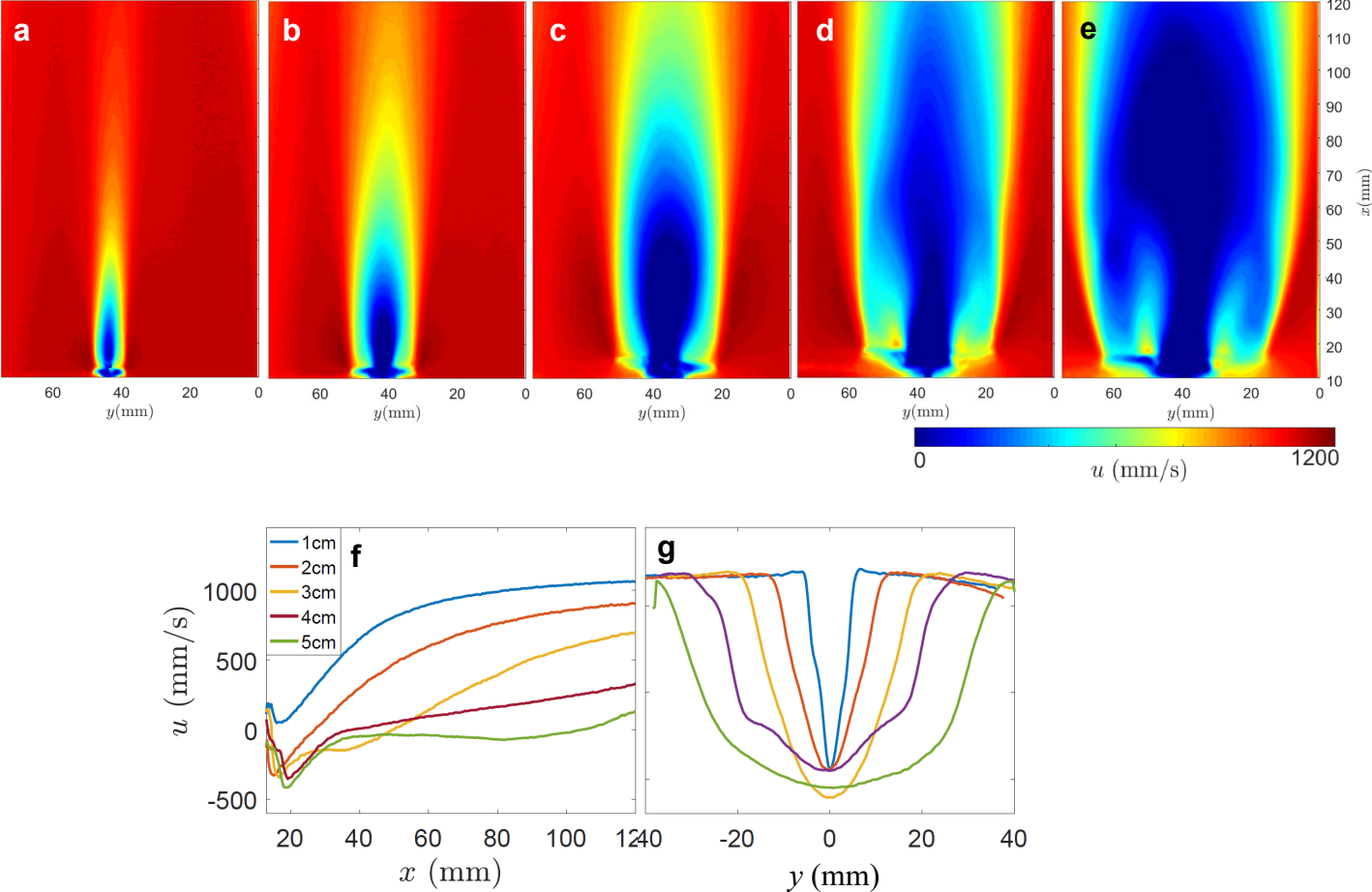
Figure S30. PIV results for 3D IoT macrofliers. Mean velocity field of (a) 1 cm, (b) 2 cm, (c) 3 cm, (d) 4 cm, and (e) 5 cm-diameter 3D IoT macrofliers at an incoming velocity $U = 1.2$ m/s. Velocity profiles along the (f) center-axis and (g) spanwise direction at a position corresponding to 12 flier diameters downstream. The results show characteristics of self-similarity.
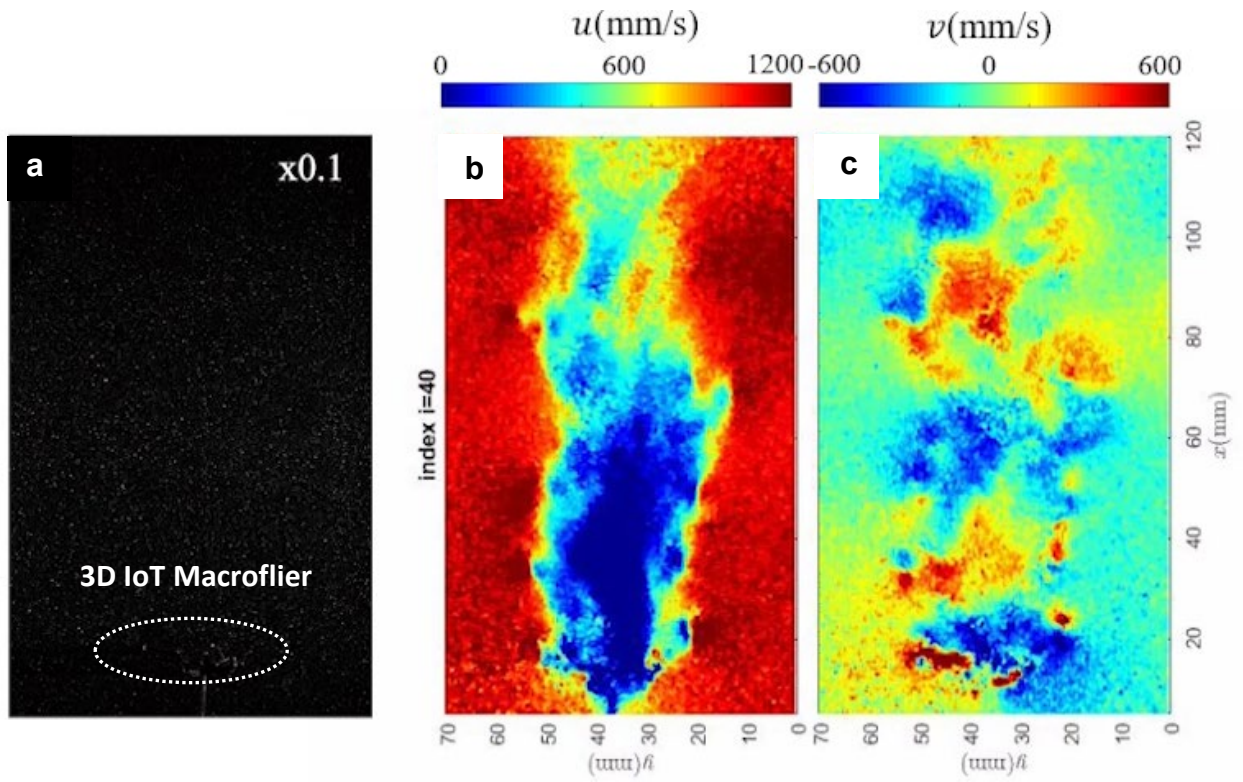
Figure S31. High-speed PIV flow measurements for 3D IoT macrofliers. (a) raw image sequence, (b) vertical velocity field, and (c) horizontal velocity field.

Supplementary Note 1: Analytic Model for 3D Rotational Falling Fliers

The aerodynamic behavior of a flier of the sort considered in this paper represents a complex structure-fluid interaction problem. As a simplification, we consider the system in a stable flying state, i.e., with a constant terminal velocity v_T and a constant rotating speed ω_T. These two key parameters that describe the falling behavior of fliers depend strongly on both the properties of the air (e.g., air density ρ, dynamic viscosity μ, etc.) and the geometry of flier (e.g., 3D configuration, tilted angle of blades, area, etc.):

$$(v_T, \omega_T) = f \begin{pmatrix} \text{air properties} \\ \text{flier geometry} \end{pmatrix}, \tag{S1.1}$$

Herein, we use a representative simplified model to parametrically characterize the geometry of the flier, which has several blades (number of n) evenly located at a radius r from the center point (Fig. 2a). Each blade is tilted by an angle β, and has a chord length c, in-plane width b and thickness t_m. The density of the flier material is ρ_m. We assume that the blade width b is small comparing to the radius r ($b \ll r$).

Focusing on the side view of a single blade (Fig. 2a, bottom enlarged subplot), the air flow is of velocity U, which can be decomposed into a vertical component v_T and a horizontal component $\omega_T r$. This problem now corresponds to a 2D airfoil (side cross-section of blade) with a coming air flow of velocity U and attack angle α, where

$$U = \sqrt{v_T^2 + (\omega_T r)^2}, \tag{S1.2}$$

$$\alpha = 90^o - \beta - \arctan\left(\frac{\omega_T r}{v_T}\right). \tag{S1.3}$$

The drag force F_D along the direction of airflow and lift force F_L perpendicular to the direction of airflow can be expressed as

$$F_D = bc \cdot C_{D(b)} \cdot \frac{1}{2}\rho U^2, \tag{S1.4}$$

$$F_L = bc \cdot C_{L(b)} \cdot \frac{1}{2}\rho U^2, \tag{S1.5}$$

where $C_{D(b)}$ and $C_{L(b)}$ are the drag coefficient and lift coefficient of the airfoil, respectively, which can be obtained by 2D CFD simulations of airfoils (Fig. S3). Decomposing the drag force and the lift force into the rotational and vertical directional forces (F_θ and F_z) yields

$$F_\theta/n = F_D \cdot \frac{\omega_T r}{U} - F_L \cdot \frac{v_T}{U}, \tag{S1.6}$$

$$F_z/n = F_D \cdot \frac{v_T}{U} + F_L \cdot \frac{\omega_T r}{U}. \tag{S1.7}$$

The force equilibrium condition is given by

$$F_\theta = 0, \tag{S1.8}$$

$$F_z = W, \tag{S1.9}$$

under the assumption $b \ll r$, where W is the weight of flier.

1. Rotating speed

With the horizontal equilibrium condition $F_\theta = 0$, Eq. (S1.6) yields

$$\frac{\omega_T r}{v_T} = \frac{C_{L(b)}}{C_{D(b)}} = L_D, \tag{S1.10}$$

where L_D is the lift-to-drag coefficient of the airfoil, which depends on the airfoil geometry, Reynolds' number (Re) and the attack angle (α) of the coming air flow (see Supplementary Figure S5b). For a given airfoil geometry under a certain Reynolds' number, Eq. (S1.10) yields

$$\frac{\omega_T r}{v_T} = L_D \left(90° - \beta - \text{atan}\left(\frac{\omega_T r}{v_T}\right)\right). \tag{S1.11}$$

The value of $\frac{\omega_T r}{v_T}$ can be solved by this implicit equation (S1.11) for a given tilt angle β. Moreover, this suggests the scaling law

$$\omega_T \propto \frac{v_T}{r}, \tag{S1.12}$$

that the rotating speed of flier is proportional to its terminal falling velocity over radius.

2. Terminal velocity

Equation (S1.7) yields

$$F_z = \frac{1}{2}\rho v_T^2 \cdot [nbc] \cdot C_{D(b)} \cdot (1 + L_D^2)^{\frac{3}{2}}. \tag{S1.13}$$

Rewriting Eq. (S1.13) with the drag coefficient of flier C_D yields

$$F_z = \frac{1}{2}\rho v_T^2 \cdot A \cdot C_D, \tag{S1.14}$$

where $C_D = C_{D,b} \cdot (1 + L_b^2)^{\frac{3}{2}}$, and $A = nbc$ is the total membrane area of flier. The drag coefficient of the flier is affected by both the drag coefficient and lift-to-drag ratio of its blade.

3. Considering the effect of Reynolds' number on drag coefficient

The drag coefficient of blade ($C_{D(b)}$) saturates at high Re, but at small Re it is nearly proportional to $\frac{1}{\text{Re}}$. The simulation results of drag coefficient of a flat airfoil versus Reynolds' number are presented in Fig. S7a. The CFD simulation results can be fitted by the function

$$C_{D(b)} \approx G_{0(b)} + \frac{G_{1(b)}}{\text{Re}}, \tag{S1.15}$$

where $(G_{0(b)}, G_{1(b)}) = (0.50, 8.3)$ for $\alpha = 30°$ and $(G_{0(b)}, G_{1(b)}) = (1.15, 10)$ for $\alpha = 60°$. Substitution of Eq. (S1.15) into Eq. (S1.13) gives

$$F_z = \frac{1}{2}\rho v_T^2 \cdot [nbc] \cdot \left(G_{0(b)} + \frac{G_{1(b)}}{\text{Re}}\right) \cdot (1 + L_D^2)^{\frac{3}{2}}. \tag{S1.16}$$

We define η as the area fill factor of flier, according to

$$\eta = \frac{A}{\pi r^2} = \frac{nbc}{\pi r^2}. \tag{S1.17}$$

With Eq. (S1.17), the Eq. (S1.16) can be rewritten as

2

$$F_z = \frac{1}{2}\rho v_T^2 \cdot \pi r^2 \eta \cdot \left(G_{0(b)} + \frac{G_{1(b)}}{\mathrm{Re}}\right) \cdot (1 + L_D^2)^{\frac{3}{2}}. \tag{S1.18}$$

when $\eta \ll 1$. Recall that $\mathrm{Re} = \rho v \cdot 2r/\mu$, Eq. (S1.18) yields

$$F_z = \frac{1}{2}\rho v_T^2 \cdot \pi r^2 \eta \cdot G_0 \tag{S1.19}$$

for large Re, where $G_0 = G_{0(b)}(1 + L_D^2)^{3/2}$. Likewisely, for small Re, Eq. (S1.18) yields

$$F_z = \frac{1}{4}\mu v_T \cdot \pi r \eta \cdot G_1, \tag{S1.20}$$

where $G_1 = G_{1(b)}(1 + L_D^2)^{3/2}$. Again, Eqs. (S1.19) and (S1.20) requires the assumption that $\eta \ll 1$.

4. Modification of theory by the extension of fill factor η

The above analysis is based on the assumption that the fill factor η is small ($\eta \ll 1$). To extend the model to practical cases where the fill factor can be larger (e.g., close to 1 in the range of $[0,1]$), we simulated the simplified flier model with various fill factors (Fig. S5). It was shown that the linear relation between F_z and η is true only for $\eta < 0.2$. For larger η the theory must be amended by changing the fitting law to $F_z \propto \sqrt{\eta}$. Therefore, the amended model is given by

$$F_z = \frac{1}{2}\rho v_T^2 \cdot \pi r^2 \sqrt{\eta} \cdot C_D. \tag{S1.21}$$

5. Effect of self-weight and load on terminal falling velocity

The weight of flier consists of two parts, i.e., self-weight (W_{self}) and load (W_{load}), as given by

$$W = W_{\mathrm{self}} + W_{\mathrm{load}} = \rho_m t_m g \pi r^2 \eta + W_{\mathrm{load}}, \tag{S1.22}$$

where ρ_m is the density of the structural material, t_m is the thickness, and g is the gravity acceleration. Substitution of Eqs. (S1.9) and (S1.22) into (S1.21) yields

$$\rho_m t_m g \pi r^2 \eta + W_{\mathrm{load}} = \frac{1}{2}\rho v_T^2 \cdot \pi r^2 \sqrt{\eta} \cdot C_D. \tag{S1.23}$$

For macrofliers, the terminal velocity is given by

$$v_T = \left[\frac{2}{\rho G_0}\left(\rho_m t_m g \sqrt{\eta} + \frac{W_{\mathrm{load}}}{\pi r^2 \sqrt{\eta}}\right)\right]^{\frac{1}{2}}. \tag{S1.24}$$

For microfliers, the terminal falling velocity is

$$v_T = \frac{4}{\mu G_1}\left(\rho_m t g r \sqrt{\eta} + \frac{W_{\mathrm{load}}}{\pi r \sqrt{\eta}}\right). \tag{S1.25}$$

This equation indicates the existence of an optimal fill factor, i.e., $\eta_{\mathrm{optimal}} = W_{load}/\pi r^2 \rho_m t_m g$, that minimizes the terminal velocity for a given W_{load}.

Supplementary Note 2: Effect of Porosity on Terminal Velocity

The idea of utilizing porosity to reduce the terminal falling velocity arises from structures in nature (Fig. S8a). For example, feathers consist of micro-fibers, between which there are void spaces. The aerodynamic properties of feathers are still very good even with these void spaces. The benefits of the void spaces are in significant reductions in the overall weight. Another example is dandelion seeds, with similar micro-fiber structures but even more void spaces, with capabilities for exceptionally low terminal velocities. Here, we explored the possibility of adding porosity into the fliers (Fig. S8b&c) to reduce these velocities. The porosity (i.e., p) is defined by

$$p = A_{\text{void}}/A_0, \tag{S2.1}$$

where A_{void} is the area of voids and A_0 is the area of a void-free flier. The area with voids present is

$$A = A_0 - A_{\text{void}} = A_0(1-p), \tag{S2.2}$$

We consider a representative 2D flat airfoil, for which the CFD simulations reveal that the porosity leads to an increase in the drag coefficient $C_{D(b)}$ by increasing $G_{0(b)}$ and $G_{1(b)}$, recall Eq. (S1.2), as shown in Fig. Sd&e, and can be fitted analytically by

$$\frac{G_{0(b)}(p)}{G_{0(b)}(p=0)} \approx \frac{1-0.95p^2}{1-p}, \tag{S2.3}$$

$$\frac{G_{1(b)}(p)}{G_{1(b)}(p=0)} \approx \frac{1-0.3p}{1-p}. \tag{S2.4}$$

Eqs. (S2.3) and (S2.4) indicate that $G_{1(b)}$ increases faster than $G_{0(b)}$ with porosity. This behavior can be explained by the flow fields near the porous airfoil, as shown in Fig. S9. At low Re, the boundary layer surrounding the airfoil, which can be seen as a virtual airfoil, is not affected by the porosity on the flat airfoil. The drag force acting on the airfoil, is therefore not significantly decreased. However, at large Re, the thickness of boundary layer is comparable to the size of void, such that the drag force decreases similarly to the area as porosity increases.

Therefore, per Eqs. (2) and (3), the knock-down factor of porosity on v_T for a microflier is given by

$$\frac{v_T(p)}{v_T(p=0)} = \frac{1-p}{1-0.3p}, \tag{S2.5}$$

and for a macroflier, the terminal velocity knock-down factor is

$$\frac{v_T(p)}{v_T(p=0)} = \sqrt{\frac{1-p}{1-0.95p^2}}, \tag{S2.6}$$

as validated by the falling tests as shown in Fig. S10.

Supplementary Note 3: Effect of Attack Angle on the Drag Coefficient of 2D Flat Airfoil

The tilt angle β affects the terminal velocity through the attack angle (α). A larger β indicates a smaller G_0 and G_1 (Fig. S7) due to its smaller attack angle ($\alpha = 90° - \beta - \text{atan}\frac{\omega_T \xi}{v_T}$, for the point on the flier at radius $\xi \in [0, r]$), and therefore leads to a larger v_T. For a large flier, the lift-to-drag ratio (L_D) of the blade can also increase significantly with small attack angle. Therefore, a small tilt angle can increase the flier drag coefficient through L_D, per Eq. (1.13), that $C_D = C_{D(b)} \cdot (1 + L_D)^{\frac{3}{2}}$. However, the lift-to-drag coefficient for a microflier is very small such that only the drag coefficient of blade plays an important role. Therefore, optimizing the tilt angle is not helpful for microscale fliers.

The 2D (two-dimensional) airfoil is the cross section of a blade for a 3D flier. Figure S7a shows the CFD simulated (see details in Methods and Fig. S3b) drag coefficient of a 2D flat airfoil (i.e., $C_{D(b)}$) versus Reynolds number, where the subscript '(b)' denotes the 'blade'. The drag coefficient of the airfoil, as defined by

$$C_{D(b)} = \frac{F_D}{A \cdot \frac{1}{2}\rho v^2}, \tag{S3.1}$$

where A is the area of the airfoil (per unit depth). $C_{D(b)}$ can be empirically given by

$$C_{D(b)} \approx G_{0(b)} + \frac{G_{1(b)}}{\text{Re}}, \tag{S3.2}$$

where $G_{0(b)}$ and $G_{1(b)}$ are the fitting parameters. Notably, Eq. (S1.2) indicates that $C_{D(b)}$ is dominated by $G_{0(b)}$ at high Re, but is dominated by $G_{1(b)}$ at low Re. In other words, $G_{0(b)}$ and $G_{1(b)}$ stand for the viscous and inertia effects of the flow, respectively (Fig. S7b). To investigate the effect of attack angle (α) on $C_{D(b)}$, we first study the effect on $G_{0(b)}$ and $G_{1(b)}$, as presented in Fig. S7c&d, which can be analytically fitted by

$$G_{0(b)} \approx 0.435 \sin \alpha + 1.02 \sin^2 \alpha, \tag{S3.3}$$

$$G_{1(b)} \approx 7.38 + 3.50 \sin^2 \alpha . \tag{S3.4}$$

Substitution of Eqs. (S1.3) and (S1.4) into Eq. (S1.2) gives the drag coefficient as a function of α

$$C_{D(b)} \approx 0.435 \sin \alpha + 1.02 \sin^2 \alpha + \frac{1}{\text{Re}}(7.38 + 3.50 \sin^2 \alpha). \tag{S3.5}$$

Supplementary Note 4: Stability analysis of rotating-falling fliers (spinners)

The stability of the rotating-falling state of the flier is analyzed by simplifying the flier as a rigid body and considering the influence of air flow. Generally, the rotational movement for a rigid body can be described as

$$\boldsymbol{\omega} = \omega_1 \boldsymbol{e_1} + \omega_2 \boldsymbol{e_2} + \omega_3 \boldsymbol{e_3}, \tag{S4.1}$$

where $\boldsymbol{\omega}$ is the rotating velocity of the rigid body, $\boldsymbol{e_1}$, $\boldsymbol{e_2}$ and $\boldsymbol{e_3}$ are the three-dimensional unit vectors of the rotating coordinate along with the rigid body, and ω_1, ω_2 and ω_3 are the rotating speed components. Euler's rotation equations take the general form:

$$T_1 = I_1 \dot{\omega}_1 - (I_2 - I_3)\omega_2 \omega_3$$
$$T_2 = I_2 \dot{\omega}_2 - (I_3 - I_1)\omega_3 \omega_1, \tag{S4.2}$$
$$T_3 = I_3 \dot{\omega}_3 - (I_1 - I_2)\omega_1 \omega_2$$

where I_1, I_2 and I_3 are assumed to be the principal moments of inertia, and $\boldsymbol{T} = (T_1, T_2, T_3)$ is the torque on the body. Consider the flier as a rigid body free falling in the air (air density ρ, dynamic viscosity μ) at a terminal velocity v_T, and rotating with an angular speed ω_T along the z direction, where the rotational movement is given as

$$\boldsymbol{\omega} = \omega_T \boldsymbol{e_3}. \tag{S4.3}$$

If a perturbation is applied on the flier and causes a slight tilt angle on 1 and 2 directions (Fig. 2f) as Λ_1 and Λ_2, respectively, then the angular velocity becomes

$$\boldsymbol{\omega} = \dot{\Lambda}_1 \boldsymbol{e_1} + \dot{\Lambda}_2 \boldsymbol{e_2} + \omega_3 \boldsymbol{e_3}, \tag{S4.4}$$

where Λ_1 and Λ_2 are both assumed to be small. Euler's equations (S4.2) take the form

$$T_1 = I_1 \ddot{\Lambda}_1 - (I_2 - I_3)\dot{\Lambda}_2 \omega_3$$
$$T_2 = I_2 \ddot{\Lambda}_2 - (I_3 - I_1)\omega_3 \dot{\Lambda}_1. \tag{S4.5}$$
$$T_3 = I_3 \dot{\omega}_T - (I_1 - I_2)\dot{\Lambda}_1 \dot{\Lambda}_2$$

Consider the torque of the air flow on the flier body as

$$\boldsymbol{T} = \boldsymbol{T}(\Lambda, \dot{\Lambda}). \tag{S4.6}$$

For small perturbations off the balanced state as

$$\delta \boldsymbol{T} = \frac{\partial \boldsymbol{T}}{\partial \Lambda} \delta \Lambda + \frac{\partial \boldsymbol{T}}{\partial \dot{\Lambda}} \delta \dot{\Lambda}. \tag{S4.7}$$

The dependence of torque T on angle perturbation $\delta \Lambda$ is given by

$$\frac{\partial \boldsymbol{T}}{\partial \Lambda} \delta \Lambda = -W d \cdot \delta \Lambda, \tag{S4.8}$$

where d is the distance between the center of pressure and center of gravity. The dependence of torque on angular speed perturbation is

$$\frac{\partial T}{\partial \dot{\Lambda}} \delta \dot{\Lambda} = - \iint_S \frac{df_D}{dv} \delta v \cdot \xi dS, \tag{S4.9}$$

in which dS is the unit area of the flier locates at radius ξ, and f_D is the drag force per unit area acting on the flier as given by

$$f_D(v) = \frac{1}{2}\rho v^2 \cdot \frac{1}{\sqrt{\eta}} \cdot \left(G_0 + \frac{G_1}{\text{Re}}\right), \tag{S4.10}$$

The velocity perturbation δv is

$$\delta v = \frac{\xi}{r} \delta \Lambda. \tag{S4.11}$$

Substitution of Eq. (S4.10) and (S4.11) into equation (S4.9) gives

$$\frac{\partial T}{\partial \dot{\Lambda}} \delta \dot{\Lambda} = - \iint_S \frac{d}{dv}\left[\frac{1}{2}\rho v^2 \cdot \frac{1}{\sqrt{\eta}} \cdot \left(G_0 + \frac{G_1}{\text{Re}}\right)\right]\frac{\xi}{r} \delta \Lambda \cdot \xi dS. \tag{S4.12}$$

Under the assumption that the area distribution of microflier is uniform at radius r, Eq. (S4.12) yields

$$\frac{\partial T}{\partial \dot{\Lambda}} \delta \dot{\Lambda} = - \frac{\pi}{8}\frac{\mu r^2}{\sqrt{\eta}} \text{Re}\left(2G_0 + \frac{G_1}{\text{Re}}\right)\delta \dot{\Lambda}, \tag{S4.13}$$

Substitution of equations (S4.8) and (S4.13) into (S4.5) and (S4.7), yields the control equations

$$I_1\ddot{\Lambda}_1 - (I_2 - I_3)\dot{\Lambda}_2\omega_T + \frac{\pi}{8}\frac{\mu r^2}{\sqrt{\eta}} \cdot \text{Re}\left(2G_0 + \frac{G_1}{\text{Re}}\right)\dot{\Lambda}_1 + Wd\Lambda_1 = 0, \tag{S4.14}$$

$$I_2\ddot{\Lambda}_2 - (I_3 - I_1)\dot{\Lambda}_1\omega_T + \frac{\pi}{8}\frac{\mu r^2}{\sqrt{\eta}} \cdot \text{Re}\left(2G_0 + \frac{G_1}{\text{Re}}\right)\dot{\Lambda}_2 + Wd\Lambda_2 = 0, \tag{S4.15}$$

Rewriting them in matrix form and normalized as

$$\begin{pmatrix} \ddot{\Lambda}_1 \\ \ddot{\Lambda}_2 \end{pmatrix} + \begin{pmatrix} \beta_0 & \omega_1 \\ -\omega_2 & a\beta_0 \end{pmatrix}\begin{pmatrix} \dot{\Lambda}_1 \\ \dot{\Lambda}_2 \end{pmatrix} + \begin{pmatrix} \gamma & 0 \\ 0 & a\gamma \end{pmatrix}\begin{pmatrix} \Lambda_1 \\ \Lambda_2 \end{pmatrix} = 0, \tag{S4.16}$$

where $\beta_0 = \frac{\pi}{8}\frac{\mu r^2}{\sqrt{\eta}} \cdot \text{Re}\left(2G_0 + \frac{G_1}{\text{Re}}\right)\frac{1}{I_1}$, $\omega_1 = \frac{I_3 - I_2}{I_1}\omega_t$, $\omega_2 = \frac{I_3 - I_1}{I_2}\omega_T$, $a = \frac{I_1}{I_2}$ and $\gamma = \frac{Wd}{I_1}$. For the extreme case that the flier is highly symmetric and $a = 1$, Eq. (S4.16) becomes

$$\begin{pmatrix} \ddot{\Lambda}_1 \\ \ddot{\Lambda}_2 \end{pmatrix} + \begin{pmatrix} \beta_0 & \omega_0 \\ -\omega_0 & \beta_0 \end{pmatrix}\begin{pmatrix} \dot{\Lambda}_1 \\ \dot{\Lambda}_2 \end{pmatrix} + \begin{pmatrix} \gamma & 0 \\ 0 & \gamma \end{pmatrix}\begin{pmatrix} \Lambda_1 \\ \Lambda_2 \end{pmatrix} = 0, \tag{S4.17}$$

where $\omega_0 = \omega_1 = \omega_2$. Equation (S3.17) can by diagonalized by the transformation

$$\begin{pmatrix} \alpha_1 \\ \alpha_2 \end{pmatrix} = \begin{pmatrix} i & -i \\ 1 & 1 \end{pmatrix}\begin{pmatrix} \Lambda_1 \\ \Lambda_2 \end{pmatrix}, \tag{S4.18}$$

that

$$\begin{pmatrix} \ddot{\alpha}_1 \\ \ddot{\alpha}_2 \end{pmatrix} + \begin{pmatrix} \beta_0 - \omega_0 i & 0 \\ 0 & \beta_0 + \omega_0 i \end{pmatrix}\begin{pmatrix} \dot{\alpha}_1 \\ \dot{\alpha}_2 \end{pmatrix} + \begin{pmatrix} \gamma & 0 \\ 0 & \gamma \end{pmatrix}\begin{pmatrix} \alpha_1 \\ \alpha_2 \end{pmatrix} = 0. \tag{S4.19}$$

This is a decoupled oscillation equation with damping, of which the 4 eigenvalues are

$$\lambda_{1,2} = -\frac{1}{2}(\beta_0 - \omega_0 i) \pm \sqrt{\left(\frac{\beta_0 - \omega_0 i}{2}\right)^2 - \gamma}, \tag{S4.20}$$

$$\lambda_{3,4} = -\frac{1}{2}(\beta_0 + \omega_0 i) \pm \sqrt{\left(\frac{\beta_0 + \omega_0 i}{2}\right)^2 - \gamma}, \tag{S4.21}$$

which can be normalized as

$$\lambda_{1,2} = -\frac{\beta_0}{2}\left[\left(1 - \frac{\omega_0}{\beta_0}i\right) \pm \sqrt{\left(1 - \frac{\omega_0}{\beta_0}i\right)^2 - \frac{4\gamma}{\beta_0^2}}\right], \tag{S4.22}$$

$$\lambda_{3,4} = -\frac{\beta_0}{2}\left[\left(1 + \frac{\omega_0}{\beta_0}i\right) \pm \sqrt{\left(1 + \frac{\omega_0}{\beta_0}i\right)^2 - \frac{4\gamma}{\beta_0^2}}\right]. \tag{S4.23}$$

The stability of the solution (i.e., $\Lambda \to 0$ when $t \to +\infty$) requires that all real part of the eigenvalues are negative. Define Γ as the stability factor as

$$\Gamma \equiv \min\left[-\frac{2\text{Real}(\lambda_{1,2,3,4})}{\beta_0}\right] = \min\left[\text{Real}\left(\left(1 \pm \frac{\omega_0}{\beta_0}i\right) \pm \sqrt{\left(1 \pm \frac{\omega_0}{\beta_0}i\right)^2 - \frac{4\gamma}{\beta_0^2}}\right)\right]. \tag{S4.24}$$

The stability condition requires $\Gamma > 0$.

The solution of Eq. (S4.17) is expressed as

$$\Lambda(t) = \sum_{i=1}^{4} C_i e^{\lambda_i t}. \tag{S4.25}$$

The amplitude of oscillation (Λ_{amp}) decays with time as

$$\Lambda_{\text{amp}} \propto \Lambda_0 \exp\left(-\frac{\beta_0}{2}\Gamma t\right), \tag{S4.26}$$

where Λ_0 is the amplitude of the initial perturbation. Therefore, a larger Γ means the amplitude decays faster that the flier can recover to its balanced stable state faster.

Substitution of $v_T = -\frac{\mu G_1}{4r\rho G_0} + \sqrt{\left(\frac{\mu G_1}{4r\rho G_0}\right)^2 + \frac{2W}{\rho A G_0}}$ into $\omega_T \propto v_T/r$ suggests that reducing r increases ω_T. Therefore, increasing d (distance between the center of gravity and the center of pressure) and/or decreasing r (size) can improve the stability through increases in $4\gamma/\beta_0^2$ and ω_0/β_0, respectively.